Geochemical fingerprints of brannerite (UTi 2 O 6): an integrated study

Marion Turuani, Flavien Choulet, Aurélien Eglinger, Philippe Goncalves, Julie Machault, Julien Mercadier, Anne-Magali Seydoux-Guillaume, Stephanie Reynaud, Fabien Baron, Daniel Beaufort, et al.

Geochemical fingerprints of brannerite (UTi_2O_6): an integrated study

Marion Turuani,[1,2] Flavien Choulet,[1,*] Aurélien Eglinger,[3] Philippe Goncalves,[1] Julie Machault,[1] Julien Mercadier,[3] Anne-Magali Seydoux-Guillaume,[2,4] Stephanie Reynaud[5], Fabien Baron,[6] Daniel Beaufort,[7] Yann Batonneau,[7] Sophie Gouy,[8], Adel Mesbah,[9] Stéphanie Szenknect,[9] Nicolas Dacheux,[9] Virginie Chapon,[10] Maurice Pagel[11]

[1]- Chrono-environnement, UMR 6249, CNRS ‑ Université de Bourgogne Franche-Comté, Besançon, France

[2]- Université de Lyon, UJM-Saint-Etienne, CNRS, UCA, IRD, LMV UMR 6524, Saint-Etienne, France

[3]- GeoRessources, Université de Lorraine-CNRS-CREGU, 54500 Nancy, France

[4]- Université de Lyon, UCBL, ENSL, CNRS, LGL-TPE, 69622 Villeurbanne, France

[5]- Université de Lyon, UJM-Saint-Etienne, CNRS, Institut d'Optique Graduate School, Laboratoire Hubert Curien UMR 5516, F-42023 Saint-Etienne, France.

[6] – LPG UMR6112 Université de Nantes – CNRS, Nantes, France

[7] - Université de Poitiers, CNRS UMR 7285 IC2MP, HydrASA Bât. B35, rue Michel Brunet, 86073 Poitiers Cedex 9, France

[8] - GET, UMR 5563 CNRS, Université Paul Sabatier, 14 Avenue Edouard Belin, 31400 Toulouse, France

[9]- CEA, CNRS, Aix-Marseille Université, UMR 7265 Biologie Végétale et Microbiologie Environnementales, Laboratoire des Interactions Protéine Métal, Saint-Paul-lez-Durance, France

[10]- ICSM, CEA, CNRS, ENSCM, Univ Montpellier, Site de Marcoule - Bât. 426, BP 17171, 30207 Bagnols-sur-Cèze, France

[11]- GEOPS, Univ Paris Sud, CNRS, Université Paris-Saclay, Rue du Belvédère, Bât. 504, Orsay F-91405, France

*: flavien.choulet@univ-fcomte.fr

Abstract

Brannerite (UTi_2O_6) is among the major uranium-bearing minerals found in ore deposits, but as it has been long considered as a refractory mineral for leaching, it is currently disregarded in ore deposits. Brannerite is found in a variety of geological environments including hydrothermal and pegmatitic, which represent the most frequent occurrences. Based on scanning electron microscopy (SEM) observations coupled with electron probe micro-analyzer (EPMA) and laser ablation inductively-coupled plasma mass spectrometer (LA-ICPMS) analyses, this study describes the morphological features and the chemical contents and trace element abundances of brannerite samples from five hydrothermal and five pegmatitic localities across the world. Mineral chemistry is also compared with transmission electron microscopy (TEM) observation and Raman spectrometry, which show that brannerite is amorphous. Major results include the definition of substitution trends and REE patterns, which are characteristics of either an occurrence or a genetic type (hydrothermal and pegmatitic). Hence, combining the major results, it is possible to obtain reliable constraints for establishing a geochemical classification of brannerite. Inferred fingerprints have direct implications for forensic science and the exploration industry; they also contribute to better understanding the metallogenic processes and optimizing the extraction of uranium.

KEYWORDS: brannerite, fingerprints, hydrothermal, pegmatite, mineral chemistry

Introduction

Growing demand for energy requires a diversification of primary raw materials as well as a re-evaluation of low grade ores, which may occur in large tonnage deposits. Current primary ores processed in the nuclear industry mostly include uraninite (UO_2) and coffinite $U(SiO_4)_{1-x}(OH)_{4x}$. Unconventional target ores include brannerite, a uranium titanate (UTi_2O_6), because of its high U content of up to 55 wt% U (Patchett and Nuffield, 1960; Skymanski and Scott, 1982). Worldwide, brannerite is reported in a variety of geological environments including sedimentary (*e.g.* Witwatersrand, South Africa; Smits, 1984), hydrothermal (*e.g.* Chateau-Lambert, France; Branche *et al.,* 1952), magmatic (*e.g.* Crocker's Well, Australia; Ludwig and Cooper, 1984) and metamorphic (*e.g.* San Bernardino county, USA; Hewett *et al.,* 1957) settings. In some deposits, brannerite is the main U-bearing mineral, like at Elliot Lake, Canada (Szymanski and Scott, 1982), Mount Isa, Australia (Wilde *et al.,* 2013) and Olympic Dam, Australia (Macmillan *et al.,* 2017). In the Witswatersrand conglomerate, brannerite accounts for 8 to 19 wt% of the total uranium mineralization (Lottering *et al.,* 2008). While U can be easily extracted from oxide minerals, brannerite has long been considered as refractory to direct leaching and for this reason it has not to date been extensively mined and/or processed (Vance *et al*., 2000, and references therein). Recent advances in hydrometallurgy have shown that U can be recovered from brannerite using acid solutions under physical- and chemical-controlled conditions (Charalambous *et al*., 2014). Uranium recovery from brannerite is not a straightforward process and the efficiency of recovery is strongly influenced by the ore paragenesis (Lottering *et al*., 2008; Sapsford *et al*., 2012). Although brannerite is

formed in a large variety of geological environments, its crystal chemistry and petrogenesis remains under-investigated.

Brannerite crystallizes in the monoclinic system, with space group C2/m (Szymanski and Scott, 1982). The general formula is best described to be AB_2O_6, where A is U and B is Ti. Both A and B sites are distorted octahedra (six-coordinated), which share corners and/or edges to form a structural framework (Szymanski and Scott, 1982, Fig. 1). Natural brannerite is commonly non-stoichiometric, and exhibits variable compositions related to more or less complex substitution mechanisms (Ditz *et al*., 1990; Lumpkin *et al*., 2012; Macmillan *et al*., 2017). The A site is mainly occupied by U, Ca, Th and rare earth elements (REE), whereas the B site includes Ti, Al and Fe. Due to the high content of radioactive elements (U, locally Th and their daughter elements), the self-irradiation of natural brannerite causes significant structural damage leading to the amorphization of the crystal lattice (Smith, 1984; Lumpkin *et al*., 2012). Such processes lead to favourable conditions for fluid circulation that contributes to the inception of alteration (Seydoux-Guillaume *et al*., 2015; Duran *et al*., 2016) and further incorporation of impurities into the brannerite structure. Such variations in composition, together with the complex nature of brannerite ores have major effects on in dissolution rates of brannerite (Goldney *et al*., 1972; Polito *et al*., 2009; Charalambous *et al*., 2012).

The detailed chemical characterization of minerals, like colombite-tantalite (Melcher *et al*., 2008) and uraninite (Mercadier *et al*., 2011; Eglinger *et al*., 2013; Frimmel *et al*., 2014) had led to classifications of minerals based on their geological environment. Such chemical fingerprints have also direct applications to the exploration industry and forensic science. Owing to the large variety of brannerite occurrences and its complex crystal chemistry, a similar chemical characterization approach is developed in this contribution. Based on both optical and electronic microscopy, major and trace element

analyses of natural brannerite minerals collected from magmatic (pegmatitic) and hydrothermal occurrences, this study aims at identifying the chemical substitutions, leading to a large variety of compositions. This characterization leads to a classification of brannerite based on the genetic type of their occurrence. This enables us to discuss implications for: (1) ore deposits fingerprints; (2) using brannerite as a dating tool; (3) determining key parameters for optimized U recovery during leaching operations.

Material and methods

Brannerite ores

The studied samples include single crystals and ores collected from hydrothermal, and pegmatitic occurrences worldwide (Fig. 2). In this section, only a brief geological overview of the sampling localities is provided; more detailed information on ore deposits or occurrences can be found in the appendix and in the referred literature. Five samples from hydrothermal occurrences were studied: La Gardette (GD) from the French Western Alps, Bou Azzer (BA) from the Moroccan Anti Atlas Belt, Chhuling Khola Valley (HL) in the Nepalese Himalaya, Mont Chemin (MC) in the Western Swiss Alps, and Kratka Valley (KV) in the Bohemian Massif. These hydrothermal veins formed after local or regional events, without direct connection to a magmatic event, and they may record a complex evolution of the fluid composition. Within veins, brannerite is spatially associated with gangue minerals within a more or less polyphase paragenetic sequence.

Five samples from magmatic-pegmatitic occurrences were studied: Crocker's Well (CW) in Central Australia, Hidden Valley (HV) in the Finders Ridge, Australia, El Cabril (EC) in the Sierra Albararrana, Andalusia, Lodrino (BR1) in the South-Central Swiss Alps and Marienfluss Valley (NA12) in Northern Namibia. These occurrences are generally dykes spatially and/or temporally associated with magmatic and metamorphic complexes. Pegmatite, which often corresponds to the last stage of the magmatic evolution, is composed of K-feldspar, quartz, albite and, among accessory minerals (listed in the appendix and in the referred literature), brannerite. For simplification, brannerite formed in magmatic-pegmatitic environments will be named "pegmatitic brannerite", while those formed in non-magmatic hydrothermal settings will be named "hydrothermal brannerite".

134

135 *Analytical methods and data processing*

136

137 Polished thin-sections and plugs were prepared from rock samples and mineral
138 chips at GeoRessources, Nancy (France). Identification of the paragenesis and textures
139 was carried out using optical microscopy and scanning electron microscopy (SEM). SEM
140 instrumentation consists of FEI Quanta 450, equipped with an EDS spectrometer and a
141 backscatter electron detector (BSE), hosted by the MIMENTO platform (RENATECH
142 Network) at the Femto-ST lab, Besançon (France). We operated at acceleration voltages
143 between 10 and 15 kV.

144 As representative of pegmatite and hydrothermal settings, respectively, two thin
145 lamellae from Lodrino and Bou Azzer samples were prepared using a FEI Helios 600i
146 FIB/SEM instrument (MANUTECH USD, Saint-Etienne, France). After localization of the
147 area of interest by backscattered electron imaging, a first 300 nm-thick protective coating
148 of platinum was deposited. A thick amorphous carbon coating was then deposited using
149 a gallium ion beam. The TEM lamellae were firstly pre-thinned at 30 kV, transferred on a
150 Cu semi grid and thinned down to be sufficiently transparent to the electron beam (*i.e.*
151 less than 100 nm). The lamellae were finally cleaned at low voltage (down to 1 kV) in
152 order to remove defects created by the FIB process and to optimize its thickness.

153 Foils were cut within the apparently unaltered (homogenous domains with limited
154 grey-scale variations under the SEM in BSE mode) domains of brannerite grains from Bou
155 Azzer and Lodrino, considered as representative of hydrothermal and pegmatitic settings.
156 Foils observations were carried out at Centre Technologique des Microstructures (CTμ)
157 in Lyon 1 University (France), with a JEOL2100F transmission electron microscope (TEM)
158 operated at 200 KeV, equipped with an energy dispersive spectrometer (SDD Oxford) and

159 a High Angle Annular Dark Field (HAADF) detector used in Scanning Transmission
160 Electron Microscopy (STEM) mode.
161 Raman microspectroscopy was performed at ambient temperature on polished
162 thin-sections and plugs at IC2MP, Poitiers (France). Raman spectra were acquired using
163 a LabRAM HR800UV confocal microspectrometer (Horiba Jobin Yvon, Villeneuve d'Ascq,
164 France) equipped with a Peltier effect-cooled CCD (Charged Coupled Device) detector.
165 The excitation wavelength was set at 632.8 nm (He-Ne laser), or at 514.5 nm (Ar^+ laser),
166 or at 532.4 nm (diode solid laser). Laser power delivered at the sample was *ca* 19 mW
167 (without filtering) and filters of optical densities of either 1 or 2 were used for all spectra.
168 Samples were analysed using a confocal high-stability BXFM Olympus microscope
169 equipped with either a 50 × LMPlan (numerical aperture: 0.55), or a 100× MPlan
170 (numerical aperture: 0.9) Olympus objective. The spatial resolution was *ca* 1×1 μm^2. The
171 spectrometer was calibrated with a pure silicon wafer using the Raman scattering line
172 centred on 520.7 cm^{-1}, which resulted in an accuracy of no less than 0.5 cm^{-1}. It consisted
173 in an 1800 grooves mm^{-1} holographic grating. Spectra were recorded in the 50-1000 cm^{-1}
174 Raman shift range with a spectral bandwidth of either 3.2 cm^{-1}(with a confocal hole
175 aperture of 200 µm at 532.4 nm), or of 8.4 cm^{-1} (with a confocal hole aperture of 400 µm
176 at 514.5 nm). Data acquisition and processing were carried out using the LabSpec version
177 5 software (Horiba Jobin Yvon).
178 Major element composition of brannerite was obtained by electron probe micro-
179 analyzer (EPMA), at GeoRessources, Nancy (France), using a Cameca SX100 equipped
180 with five wavelength dispersion spectrometers (WDS). Carbon-coated polished thin
181 sections were analysed with an acceleration voltage of 20 kV, and a current of 100 nA. The
182 spatial resolution is ca. 1 µm, with an average acquisition time of 5 minutes. Oxides,
183 silicates, and pure metals were used as standards (Table A1). In addition, quantitative and

qualitative elemental composition maps were obtained using (1) a Field-Emission Gun (FEG) Cameca SXFive FE, equipped with five WDS at Centre de MicroCaractérisation Raimond Castaing at Toulouse (France) (for samples from Himalaya and El Cabril) and (2) a JEOL 8200 Superprobe equipped with five WDS, hosted at University of Geneva (for sample from Bou Azzer), respectively. In theses cases, acceleration voltage was of 10 kV and a current of 100 nA. Elemental composition maps were produced with a resolution of 1 µm and an acquisition time of 600 ms per pixel. Following Collela *et al*. (2005), U^{4+}, U^{5+} or U^{6+} relative content was estimated on a basis of 6 oxygen atoms and 3 cations. There is no unique solution to balance charges, therefore the average valence state has been chosen as the most reliable parameter.

The minor and trace element contents were quantified using a laser ablation (193-nm excimer Geolas Q Plus System) coupled to an inductively-coupled plasma mass Spectrometer (Agilent 7500c Quadrupole) at Georessources, Nancy (France). The fluence was 5 J cm^{-2}, using a repetition rate of 5 Hz. The laser spot sizes were 24 or 32 µm in diameter, depending on the size of brannerite crystals. The total acquisition time, including background and signal was limited to 200 s per analysis, with a background acquisition of 30 s before ablating the material for 40 s. The following elements were measured: B, Mb, Al, Si, Ca, Ti, Cr, Mn, Fe, Co, Ni, Cu, Zn, Y, Nb, Mo, the REEs, Pb, Th, U with a dwell time of 10 ms (except 5 ms for U and Pb). The cycle time was 394 ms. The He flux was fixed at 0.5 $l.min^{-1}$ and 0.9 $l.min^{-1}$ of Ar was added before entering the plasma. The reference material was a SRM NIST 610 glass standard (*Pearce et al., 1997*) and Ti and/or U contents measured by EPMA on the same area were used as an internal standard. Data reduction was carried out with IOLITE software (Paton *et al*., 2011). Analytical precision is calculated for all elements analyzed using standard deviation of recorded intensity and is better than ±15% for concentrations higher than 10 ppm and becomes greater (±50%

209 to ±70%) for concentration lower than 10 ppm. Limit of detection varies for each element
210 as a function of signal intensity and was calculated for each ablation from signal
211 intensities using the 3σ criterion (Longerich *et al*., 1996). The most commonly achieved
212 LODs are below 2 ppm for the measured trace elements.

213 The comparison between chemical compositions of brannerite from different
214 deposits was achieved by estimating the difference in content of a given element (see
215 detailed procedure in Machault *et al*., 2014). For this, we first calculated the coefficient of
216 variation defined by Cv (%) = σ/μ (where σ is the standard deviation and μ is the average)
217 to describe the degree of homogeneity for the distribution of the analysed elements. The
218 non-parametric Kolmogorov–Smirnov test (*e.g.* Press *et al*., 1986) was then used to
219 compare two populations and therefore evaluate the homogeneity between two samples.
220 We also applied multivariate statistical processing, to highlight the substitution trends
221 within brannerite. The principal component analysis (PCA) is a powerful variable-
222 reduction technique, which is more and more applied to geochemical data (*e.g.* Belissont
223 *et al*., 2014). By recalculating principal components, which are defined as orthogonal
224 linear combinations of the initial variables, it is possible to project multivariate data in
225 two-dimensions with minimal data loss. The two first principal components, which are
226 used in this study, carry the highest explained variance, corresponding to the most
227 significant relationships between the variables. More detailed about PCA method can be
228 found in Koch (2012). For all calculations, we used R software and FactorMin R package
229 for PCA (Lê et al., 2008).

230

231 **Results**

232

233 *Petrography of brannerite ores*

234

235 *Hydrothermal brannerite*

236

237 Brannerite crystals from La Gardette occur as laths, associated with Bi-Cu minerals
238 (emplectite and wittichenite), native gold and quartz (Fig. 3a). A corroded boundary is
239 always observed and composed of newly formed and chemically different brannerite,
240 cerussite, REE phosphates, and iron oxides. Brannerite include minute inclusions of U-
241 rich minerals (not determined), while inclusion-free brannerite veins are also very
242 common in the studied crystals.

243 Samples from Bou Azzer exhibit elongated laths of brannerite associated with
244 quartz, barite and minor galena (Fig. 3b). Except for the presence of galena inclusions, BSE
245 images of brannerite crystals show a rather homogeneous internal structure suggesting
246 that brannerite crystals may be chemically homogeneous. However, element distribution
247 mapping reveals a complex inner structure within crystals (Fig. 4a-d), marked by the
248 presence of sub-rounded domains with varying Fe contents (Fig. 4d) Alteration also
249 occurs as partial to full replacement (Fig. 3b), marked by an intricate association of U-rich
250 and U-poor Ti oxides that coexist with coffinite and sulphate minerals (barite, anglesite)
251 (Fig. 3c).

252 Millimetre-sized anhedral crystals of brannerite from Himalaya are enclosed in
253 albite. BSE images and X-ray mapping reveal at least three distinct stages of brannerite
254 crystallization (Figs. 3d, 4e-h). The first stage (Br I) is characterized by oscillatory-zoning
255 and U, Th and Y chemical variation (Fig. 4f-h). This primary brannerite is cross-cut by two
256 successive generations of veins (Br II and Br III) that may ressemble stockwerk. These
257 veins are rich in U and poor in Y and Th. Alteration rims are very limited, but a Cu-U-

bearing arsenate, possibly (meta-) zeunerite, and unidentified phosphate minerals are commonly found around these crystals.

Brannerite from Mont Chemin occurs as small crystals (less than 150 μm), associated with anatase, biotite, K-feldspar, REE carbonates and minor uraninite inclusions. Crystals are usually prismatic and display a large rim of altered brannerite (Fig. 3e). At Kratka Valley, brannerite occurs as sub-rounded crystals within a quartz matrix. Fractures are frequent and numerous inclusions of Ti oxides and uraninite are observed (Fig. 3f). Alteration is pervasive.

In the sample from Bou Azzer, TEM-Bright Field (BF, Fig. 5a) and STEM-HAADF (High Angle Annular Dark Field) (STEM-DF, Fig. 5b) images reveal the presence of a dense network of inclusions, either enriched in U (Fig. 5c) or in Pb (Fig. 5e). Selected Area Electron Diffraction (SAED) patterns identified within brannerite and dark U-rich inclusions result in broad diffuse rings equivalent to amorphous material (inset in Fig. 5a). The only trace of nano-crystalline material within the Bou Azzer sample corresponds to the cubic-like Pb-rich inclusion, certainly galena. The amorphous state of natural hydrothermal brannerites is also evidenced by Raman microspectroscopy (Fig. A1). The Raman spectra of hydrothermal brannerite samples, acquired in unaltered domains (Fig. 3), do not exhibit the characteristic features of pure synthetic brannerite (Mesbah *et al*. 2019). The Raman spectra of brannerite samples exhibit a small but significant feature at 151 cm^{-1} (only for La Gardette sample) and broad and poorly resolved features around 600, 750, and 820 cm^{-1} (Fig. A1).

Pegmatitic brannerite

Samples from Crocker's Well display sub-rounded elongated crystals of brannerite that displays intensive microfracturation (Fig. 6a). Brannerite is associated with Ti oxides, which are also present as micrometre-sized euhedral inclusions within brannerite. Along fractures and in the rim, U-Th rich silicates (possibly uranothorite) coexist with brannerite, although no genetic relationships can be demonstrated. This association is characteristic of an altered zone, which may also display U-depleted zones (Fig. 6a) and apatite. Microfractures are filled with U-Th secondary products, which are too small to be identified with the techniques employed here.

Brannerite from Hidden Valley is a single elongated millimetre-sized crystal, which displays well-developed corroded boundaries and transversal fracturing with alteration (Fig. 6b). Preserved brannerite exhibits tiny uraninite inclusions. The rim is zoned, showing differences in U depletion; it also contains secondary U-Th minerals, which belong to the thorite-coffinite series, according to Raman spectroscopic analyses.

The studied single crystal of brannerite from El Cabril is also characterized by a pervasive corroded boundary (Fig. 6c), but we also observed the presence of parallel fractures filled with a symplectite-like association of uraninite, Ti-oxides and an unknown yttrium-rich phase (Figs. 6d, 7a-d). At sites of dilational jogs, uraninite crystals are bigger in size, but still anhedral. This fracturation/filling stage predates alteration, which occurs as a large and complex rim, surrounding the single crystal. This rim presents a succession of U-depleted domains with locally botryoidal aggregates and thin lamina of U-Ti oxides.

Euhedral prismatic brannerite crystals from Lodrino are associated with K-feldspar. They do not display any evidence of internal texture, but, locally, a complex zoned rim of altered brannerite has been observed (Fig. 6e). Brannerite from Namibia is also a single crystal, which presents a sub-rounded irregular shape. Inclusions are rare within brannerite, but fractures are locally filled with uraninite partially replaced by

307 coffinite (Fig. 6f). Interestingly, brannerite can also occurs with a collomorph texture, very
308 similar to frequently observed pitchblende (Fig. 6f).

309 In the Lodrino sample, BF-TEM and DF-STEM images show the presence of altered
310 domains within brannerite (Fig 8a-b), with a variation in composition for U, Ti, and Si (Fig.
311 8c-e). The brightest parts within this area (Fig. 8b) seem to be enriched in Si sometimes
312 correlated with U enrichment. In contrast, darker areas are depleted in U and Ti. Pristine
313 brannerite areas only reveal U and Ti. The diffraction pattern within the unaltered
314 brannerite domain indicated it is completely amorphous (inset in Fig. 8a above); in
315 contrast the diffraction pattern from the altered domain shows evidence of nano-
316 crystalline material, with two intense rings with d-spacings of 3.45 Å and 1.87 Å (inset at
317 the bottom in Fig. 8a). The amorphous state of natural pegmatite brannerites is confirmed
318 by Raman microspectroscopy (Fig. A1), since like for hydrothermal brannerite, the Raman
319 spectra acquired in unaltered domains (Fig. 6), do not exhibit the characteristic features
320 of pure synthetic brannerite (Mesbah *et al*. 2019). Again, with the exception of the well-
321 defined feature at 151 cm-1 for the sample from Namibia, only broad and poorly resolved
322 features around 600, 750, and 820 cm^{-1} (Fig. A1).

323

324 *Major and minor element content*

325

326 The composition of brannerite was obtained from domains that appear
327 homogenous and middle grey under the SEM (Figs 3, 6), away from corroded grain
328 boundaries (*e.g.* Figs. 3a, 6c) and altered domains *e.g.* along fractures (*e.g.* Figs. 6b, 6f).
329 Table 1 and boxplots of Fig. 9 summarize the distribution of major and minor element
330 contents, expressed in atom per formula unit (apfu), following Collela *et al*. (2005; see
331 section “Materials and Methods”). The measured U content is always less than 1 atom per

formula unit. While Ti content of hydrothermal brannerite ranges from 1.9 to 2.1 apfu, this value is always less than 2 apfu for pegmatitic brannerite, except for BR1.

For major and minor elements, we observe variations in chemical composition between geological settings. For instance, aluminium in hydrothermal brannerite is always lower than 0.01 apfu, while brannerite from pegmatites have wider range in Al contents. Chemical variations are also observed within a single geological environment. Ti, Fe and Y for hydrothermal brannerite show significant variations, while U, Ca and Th are the most variable components in pegmatitic brannerite. Finally, significant chemical variations are also observed for a given occurrence: *e.g.* U, Y, and Th for Himalaya and Ti, Fe and Si for Bou Azzer. Such variability of element content within a single sample is also revealed by element chemical maps, which display chemical zoning within crystals (*e.g.* U, Th and Y in brannerite from Himalaya, Fig 4e-h).

Trace element content

The trace element content may vary by several orders of magnitude depending on samples, sample locality and sample type (Table 2, Fig. 10). Trace element concentration may reflect the local geological environment, like the high chromium content in Bou Azzer that is related to the occurrence of metasomatized ophiolites hosting the deposit (Fig. 10a). In the case of Mn and Nb, no clear signature can be pointed out at the scale of deposit type (Fig. 10b-c), although the Mont Chemin sample shows high concentrations in these two elements. For metals like Cu and Zn (Fig. 10d-e), no clear trend can be observed, except local enrichment in Cu and Zn for brannerite from Mont Chemin. The Pb content distribution between samples is very heterogeneous (Fig. 10f): this may either reflect local Pb enrichment as it correlates with high Zn and Cu contents (*e.g.* Mont Chemin),

and/or enrichment due to production of radiogenic lead (as a result of elapsed time since crystallization). In this latter case, old and high U+Th brannerite like Crocker's Well and Hidden Valley have a Pb content that displays orders of magnitude higher than the youngest brannerite from Lodrino.

Principal component analysis major and minor elements

The results of the PCA applied to the EPMA dataset are displayed in Figure 8, where spot analyses (individuals, to the left) and elements (variables, to the right) are projected on the PC1 vs. PC2 plane. For the hydrothermal brannerite dataset, loadings of PC1 and PC2 represent 49.85% of the element content variability (Fig. 11a-b). The PCA plot underlines two main opposed pairs of element clusters. For the first pair mostly loaded by PC1, one group is composed of Ce, P, Y, and Nd, while the other group includes U and Th. For the second pair mostly loaded by PC2, a cluster composed of Fe, Mg, Ca and Si is opposed to Ti. Spot representation in the PC1 vs. PC2 plane refers to the sample location. PC1 (mostly loaded by U, Th, and REE) is correlated with samples from Mont Chemin and Himalaya, whereas PC2 (loaded by Ti, Ca, Fe) is correlated with samples from Bou Azzer, Kratka Valley and La Gardette.

For pegmatite samples, PC1 and PC2 represent 56% of chemical composition variations (Fig. 11c-d). The PCA also reveals some differences like Si and Th that are now observed as clusters in association with REE and P. The group of elements opposed to Ti includes Al, but not Ca, which occupies an intermediate position. All individuals are grouped, without any overlap of sample localities (Fig. 11c). As a result, two subgroups can be distinguished. While a first one (PC1 loading) including the Crocker's Well, Hidden

Valley, and El Cabril samples correlates with U, Th and REE, a second one (PC2 loading) composed of Namibia and Lodrino samples, correlates with Ti, Al and Fe.

Inferred chemical substitutions in brannerite

The EPMA analytical totals, expressed as weighted per cent of oxides (wt%) for each analysis range between 95% and 100%, except for samples from Bou Azzer (mean 92.11 wt%) and Crocker's Well (mean 92.61 wt%) samples (Table 1). This range is consistent with values provided by Charalambous (2013) and Macmillan *et al.* (2017). Totals lower than 100% can be related to several factors:

(1) Among REEs, only Ce and Nd were measured by EPMA, and both elements account for only 15 to 50% of the total REE of the sample, depending on the LREE anomaly (see section *Trace elements variation*);

(2) We assumed that EPMA-measured oxygen only occurs as O^{2-} anions within the brannerite structure. However, U (and Th) α-decays induce radiation damage leading to amorphization of the brannerite crystals as confirmed by TEM imaging (Figs. 5, 8) and the complete loss of the Raman vibrational mode (Fig. A1). The self-radiation damages (metamictization), which affect the crystal structure of brannerite can contribute to incorporation of either H_2O or OH^- (Lumpkin *et al*., 2012). These authors reported H_2O contents between 0 and 3.7 wt%, and up to 7.4 wt% in highly damaged crystals from Crocker's Well. Other deviations from ideal stoichiometry (AB_2O_6) can be achieved through vacancies or excess oxygen (Colella *et al*., 2005);

(3) Calculations of weighted oxide content assumed a unique valence for U (U^{4+}), Fe (Fe^{3+}), Ce (Ce^{3+}) and Pb (Pb^{2+}). While this is probably correct for the three latter ones, direct measurements of uranium chemical states on brannerite samples have demonstrated that

406 higher valence states (5+ and 6+) should be considered (Vance *et al*., 2000, 2001; Finnie
407 *et al*., 2003).

408 Our dataset confirms the variability of brannerite compositions reported in the
409 literature (Lumpkin *et al*., 2012; Macmillan *et al*., 2017), but in these studies, no
410 distinctions were made based on the geological environment where brannerite
411 crystallized. As shown by the respective locations of variable (elements) and individuals
412 (samples) clusters in the PCA plots (Fig. 11), chemical heterogeneity is mostly due to
413 replacement of Ti by Fe, Al and U by other cations, like Th, Ca, REE and Y with similar ionic
414 radius in 6-fold coordination sites (Shannon, 1976).

415 Uranium substitutions in the A site by Th, Ca, REE and Y account for up to 50% of
416 A site occupancy (Table 1). Substitution between U and Th is straightforward:

417 $$U^{4+} = Th^{4+} \quad (1)$$

418 But this substitution is important only in brannerites from Mont Chemin, Hidden Valley
419 and Crocker's Well (Fig. 12a-b). For other cations (Ca, REE, Y), coupled substitutions must
420 be considered to account for their incorporation (Lumpkin *et al*., 2012). The Ca content in
421 the A site is always associated with higher calculated average U valences (Fig. 12c), which
422 may reflect the following substitutions.

423 $$2U^{4+} = Ca^{2+} + U^{6+} \quad (2)$$

424 $$3U^{4+} = Ca^{2+} + 2U^{5+} \quad (3)$$

425 While the presence of U^{6+} is commonly observed in U minerals formed under oxidizing
426 conditions, the presence of U^{5+} was presumed in the Ca-rich brannerite from El Cabril
427 (Vance *et al*., 2001). René and Dolníček (2017) also proposed these substitutions to
428 explain the high Ca content of brannerite from the Bohemian Massif.

PCA analysis shows an excellent correlation between P and Y + REE (Fig. 11) suggesting that phosphorus could also be involved in the substitution of U^{4+} in the A site via the substitution:

$$2U^{4+} = (Y, REE)^{3+} + P^{5+} \quad (4)$$

Although the ionic radius of P^{5+} (0.38 Å) is very different from that of U^{4+}(0.89 Å), the partial destruction of the crystal structure of brannerite through metamictization may have favoured the incorporation of P into the octahedral coordination A site (Shannon, 1976). In our case, the REE + Y contents (up to 5 x 10^4 ppm) cannot be counterbalanced via substitution (4), because of low average P contents (10^2 ppm). The incorporation of REE and Y in the A site is also made possible by substituting and oxidizing U^{4+} into U^{5+} through substitution

$$2U^{4+} = (Y, REE)^{3+} + U^{5+} \quad (5)$$

Fig. 12c-f shows that hydrothermal brannerite from La Gardette and Himalaya are characterized by a clear relationship between Y + Ce and U^{4+} or average U valence consistent with the substitution vector of equation (5). Brannerites from pegmatites also show a correlation between U^{4+} and Y + Ce apfu, but with a different slope. This difference can be due to either unanalysed REE (and fractionation between the REE) or a different substitution mechanism. This relationship between Y + REE substitution in the A site and the genetic type has also been reported in Olympic Dam brannerite, which belongs to different generations (Macmillan *et al.*, 2017).

Composition variability of brannerite is also due to replacement of Ti by different cations up to a maximum of 25% of the B site occupancy. PCA analysis of Fig. 11 shows that Ti and Fe^{3+} +/- Al^{3+} are correlated in both hydrothermal and pegmatitic brannerite. In the pegmatitic brannerite, substitution of Ti by these tetravalent cations induces a

charge deficit on the B site that could be compensated by higher valences of U on the A site, through coupled substitutions like

$$(Fe, Al)^{3+} + U^{5+} = Ti^{4+} + U^{4+} \quad (6)$$

$$2(Fe, Al)^{3+} + U^{6+} = Ti^{4+} + 2U^{4+} \quad (7)$$

Fig. 10 shows a correlation between Ti or U average valence with $Fe^{3+} + Al^{3+}$, which is consistent with substitutions (6) and (7). The respective contribution of substitutions (2), (3), (5), (6) and (7) in the A and B sites to the average valence is difficult to ascertain, except for pegmatitic brannerite from Namibia (Fig. 13). In this case, the limited amount of Ca, REE and Y (<0.1 apfu) (Fig. 12) cannot account for the high average valence (4.63) of U that is better explained by high Fe and Al content (0.25 to 0.4 apfu; Fig. 13). Coupled substitutions involving Ti or other cations of the B site, as proposed in Lumpkin *et al*. (2012) and Macmillan *et al*. (2017) could also explain the absence of direct correlation between U and Ca in the PCA plots for hydrothermal and pegmatitic brannerite (Fig. 11).

Lumpkin *et al*. (2012) proposed an alternative substitution to compensate the charge deficit induced by the replacement of Ti by Fe and Al:

$$(Fe, Al)^{3+} + Nb^{5+} \rightarrow 2Ti^{4+} \quad (8)$$

In our case, there is no positive correlation between Fe, Al, and Nb. Fe-Al-poor hydrothermal brannerite is rich in Nb, whereas pegmatitic brannerite generally presents higher Al and Fe contents and is depleted in Nb (Figs 9c-d, 10c). MacMillan et al. (2017) also suggests that missing charges could be due to the removal of OH^- anions through the substitution $Ti^{4+} + OH^- = (Fe^{3+}, Al^{3+})$ (9), since appreciable water contents up to 7.4 wt% have been measured in natural brannerite (Lumpkin *et al*., 2012).

For hydrothermal brannerite, substitutions on the B site are limited and in many cases the calculated Ti amount exceeds 2 apfu (Fig. 13a). Such deviation was also reported in magmato-hydrothermal brannerites from Olympic Dam (Macmillan *et al*., 2017) and

478 different hypotheses can be advanced: (1) coupled substitutions across the two sites; (2)
479 nanometric inclusions of Ti oxides intergrown with brannerite, similar to macroscopic
480 structures in magmatic and metamorphic brannerite (Figs 2, 4); (3) vacancies or other
481 substituents at the anion sites, causing overestimation of the cation content in the
482 structural formula calculation; (4) alteration processes leading to a partial removal of U,
483 without changing the crystal texture at the microscale. The Raman spectra obtained from
484 La Gardette and Namibia brannerites show a very small and broad band at around 640
485 cm^{-1} and the characteristic E_g mode at 151 cm^{-1} (Fig. A1). Such features are interpreted as
486 a spectroscopic signature of nanocrystalline anatase, probably blue-shifted with regard
487 to the corresponding mode of its core crystalline counterpart, displaying a significant
488 broadening of its profile (Bonne *et al*. 2010). This is the result of the metamictization of
489 brannerite crystals, even in the unaltered domains.
490 As noted by Lumpkin *et al*. (2012) and Macmillan *et al*. (2017), there is almost no
491 correlation between Ti and Si abundances, as occupancy of octahedral sites by Si is
492 impossible in low-pressure oxide compounds (Mysen and Richet, 2005). PCA plots display
493 very heterogeneous trends for Si relative to other elements (Fig. 11). While, for
494 hydrothermal brannerite, we may note a correlation between Si and Ti, for pegmatitic
495 samples we rather observe Si opposed to U along the PC1 (Fig. 11). This suggests either
496 an addition of Si within A sites, or the presence of nanoscale U-bearing silicates such as
497 coffinite. TEM-EDS chemical mapping revealed that parts of brannerite altered domains
498 are enriched in Si and depleted in U (Fig. 8a-e).). From the SAED patterns taken in this
499 altered domain (Fig. 8a), apart from diffuse rings corresponding to amorphous material,
500 additional diffraction spots with equivalent d-spacings of 3.45 Å and 1.87 Å could
501 correspond to the (200) and (321) planes of coffinite (3.41 Å and 1.88 Å, respectively from
502 Pointeau *et al*., 2009), although those of brannerite (3.50 Å and 1.85 Å) are very close. For

503 comparison, in (Y, REE, U, Th)-(Nb-Ta-Ti) oxide minerals, altered domains were also
504 characterized by Si gain and U loss. This alteration results from fluid-mineral interaction,
505 favoured by fracturing due to radiation damage accumulated in U and Th-rich oxide
506 minerals (Duran *et al*., 2016). A very similar process probably occurs for brannerite as (1)
507 all crystals of natural brannerite are metamict (Figs. 5, 8, A1) and (2) Si-rich brannerite
508 (*e.g.* Crocker's Well and Hidden Valley) are characterized by radial fracturing and well-
509 developed altered domains (Fig. 6a-b). Further careful nanometric observations and
510 additional brannerite synthesis in Si-rich environments are necessary to better
511 understand the mechanisms for Si incorporation within brannerite.
512
513 **Brannerite fingerprints**
514
515 *Major element and substitution*
516
517 These new results show that each locality and each genetic type are characterized
518 by various types and degrees of substitution, either on the A or on the B sites (Fig. 14).
519 Fig. 14a shows that hydrothermal brannerite is mostly characterized by a predominance
520 of A site substitution (90%), while pegmatitic brannerite generally presents a higher
521 proportion (20%) of B site substitution. Pegmatitic brannerite from Namibia represents
522 an extreme case, with a predominance of B site substitution (70 to 90%). The
523 incorporation of Si, whose mechanism is not well understood, seems to increase when
524 both A and B site substitutions are present (Fig. 14a). However, this could also reflect the
525 degree of alteration and mirrors the possible modification of the initial chemical
526 composition of brannerite.

Brannerite populations can also be distinguished based on the cations incorporated in sites A and B via the substitutions described previously. In hydrothermal brannerite, except for Th-rich brannerite from Mont Chemin, A site substitution is mostly characterized by high REE + Y contents, with local enrichment in Ca such as in Bou Azzer (Fig. 14b). For pegmatitic brannerite, A site is characterized by (1) an equal distribution of Th and Y + Ce and (2) various degree of Ca substitution (Fig. 14b). In uraninite formed under hydrothermal conditions, the Th content is usually negligible as Th is less mobile and Th^{4+} displays very low solubility (Cuney and Friedrich, 1987). In magmatic environments, the Th content generally increases (*e.g.* Förster, 1999; Frimmel *et al*., 2014), except if the source of radiogenic elements (magma or protolith) is initially poor in Th. In the B site, while only Fe^{3+} replaces Ti in hydrothermal brannerite, pegmatite brannerite are characterized by the incorporation of both Fe^{3+} and Al, with an Al/Fe^{3+} ratio around 1:6 (Fig. 14c).

Strong variations in chemical composition are also observed at the scale of a given sample or locality, as exemplified by the case of Himalaya. Although morphological differences support the presence of three brannerite generations (Fig. 4e-h), their composition follows the same substitution trends (1) and (5). This suggests dissolution - reprecipitation process of brannerite without an external chemical contribution. This observation differs from the results reported at Olympic Dam, in which four generations of brannerite are related to distinct substitutaion mechanisms (Macmillan *et al*., 2017).

In addition to substitution-related fingerprints (Fig. 14), it is possible to obtain individual signatures for either the brannerite genetic type or the brannerite locality using statistical methods. The non-parametric Kolmogorov–Smirnov test was used to compare the distribution of two populations and therefore evaluate the homogeneity between two samples for a given element. The statistical analysis shows that element

552 content distributions significantly differ (at 95%) between samples, suggesting that each
553 locality has its own mineral chemistry (Fig. 15). However several samples show a weaker
554 range of differing elements, supporting that these localities are close in terms of mineral
555 chemistry (*e.g.* BA and KV or CW and HV). This is an agreement with the distribution
556 observed in PCA (Fig. 11) and classification plots (Fig. 14).
557
558 *Trace elements variation*
559
560 Fingerprints can also be deduced from trace elements measured in brannerite. As
561 mentioned in section 3.3, interpreting the trace element content (Fig. 10) is difficult as
562 some elements may either (1) be or not be associated with coupled substitution (*e.g.* Nb);
563 (2) reflect the local geological environment (Cr at Bou Azzer); (3) derive from different
564 sources (*e.g.* common versus radiogenic Pb). In the case of REE, their incorporation is
565 associated with stoichiometric rules, as ionic radii of REE are close to U, despite a relative
566 lack of knowledge of charge balance mechanisms. The shapes of REE patterns differ
567 between the two genetic types:
568 (1) Hydrothermal brannerites are marked by a bell-shape (Fig. 16a). MREE such as Tb
569 (0.92 Å), Dy (0.91 Å), Ho (0.90 Å) and Er (0.89 Å) have ionic radii very close to that of U^{4+}
570 (0.89 Å) in 6-fold coordination (Shannon, 1976) and, therefore, are most easily
571 incorporated in the brannerite structure. Similar patterns were observed for uraninites
572 formed in unconformity deposits (Pagel *et al*., 1987; Mercadier *et al*., 2011; Frimmel *et al*.,
573 2014). The total amount of REE is usually high (more than 10000 ppm) and the
574 LREE/HREE ratio oscillates between 0.3 and 3.8 (Fig. 17).
575 (2) At high temperature (>500°C), the brannerite structure dilates (Zhang *et al*., 2006)
576 allowing the incorporation of REE, without any fractionation due to differences in ionic

radii. Pegmatitic brannerites are marked by LREE depletion, or a regular decrease from HREE towards LREE (Fig. 16b). The total amount of REE shows strong variations (Fig. 17), probably due to competitive substitutions at site A (Fig. 14c). In addition to a general fractionation between LREE and HREE, it is worth noting that the fractionation rate (LREE/HREE) increases with the total amount of REE (Fig. 17).

For the same sample type or locality, the REE patterns are very consistent (Fig. 16). Minor differences may be mostly due to variations of total REE and/or a change in the europium anomaly. In most cases, the Eu anomaly is absent or slightly negative attesting for an early fractionation of Eu by feldspars, which are described in almost all mineral associations. Eu positive anomalies are reported in La Gardette and El Cabril and could be associated to a local change of redox conditions. It is noteworthy that positive anomalies in El Cabril samples tend to be associated with the high total REE analysis (Fig. 16b). Cerium also shows a frequent positive anomaly, which is also related to redox conditions (*e.g.* Mont Chemin). Under oxidizing conditions, Ce^{3+} changes to Ce^{4+}, which is preferentially incorporated in site A of brannerite, since its ionic radius (0.87 Å for Ce^{4+} in 6-fold coordination; Shannon, 1976) is close to that of U^{4+} (0.89 Å) and its addition does not require charge balance.

These results suggest, that beyond crystal-scale controls, addition of REE also depends on external parameters such as temperature, but also of the presence of other mineral phases that may trigger REE fractionation (Fig. 16c). Among them, monazite, which was reported in several brannerite-bearing samples, preferentially partition LREE and could be at the origin of the LREE-depleted patterns of most of brannerite.

Implication of brannerite systematics

Fingerprints for tracking origin of ore

Defining brannerite fingerprints offers a potential useful application in tracking down the source of possibly illegally mined uranium ores. Such an approach was applied to a variety of conflict or strategic minerals, like colombo-tantalite (Melcher *et al*., 2008, 2015), gems (Giuliani *et al*., 1998, 2005) and uraninite (Mercadier *et al*., 2011; Frimmel *et al*., 2014; Spano *et al*., 2017). Chemical fingerprints of brannerite consists of a combined characterization of the major substitution trends (A and B sites), the nature of elements incorporated, and the shape of REE patterns. Other trace elements can be used as they may represent a locality-specific feature, which may be useful in forensic studies. However, as shown by this study and reported in previous literature (*e.g.* Charalambous *et al*., 2012; Lumpkin *et al*., 2012; Macmillan *et al*., 2017), brannerite ores are generally complex and include other uranium minerals (*e.g.* uraninite, coffinite) and/or successive generations of brannerite with variable mineral chemistry (Fig. 4e-h). Hence, traceability studies cannot be done at ore scale, but require careful consideration of U-bearing mineral phases. A complementary signature using isotope systematics (O, U, Th, Pb) as proposed for uraninite (*e.g.* Pajo *et al*., 2001) could also be a useful tool to provide unequivocal source for brannerite.

Using brannerite as a tool for dating mineralizing events

The high U (and Th) abundance makes brannerite a good candidate tool for dating mineralizing events. Previous geochronology was carried out using a variety of techniques including the ID-TIMS (Ludwig and Cooper, 1984; Copeland *et al*., 1991) and the LA-ICPMS (Oberthür *et al*., 2009) over a large range of ages (4.8 Ma to 670 Ma). These

627 published geochronological data lack in most cases detailed petrography to support
628 unequivocal evidence for (1) unique brannerite chemistry close to ideal composition to
629 limit matrix effects and (2) single crystallization stage to avoid mixing between different
630 age populations. The nature of Pb is another crucial issue that needs to be considered for
631 dating application. In 6-fold coordination, the respective ionic radii of Pb^{4+} and Pb^{2+} are
632 0.77 Å and 1.19 Å, respectively (Shannon, 1976), suggesting that Pb poorly substitutes for
633 U at the A site. The dilatation of the crystal structure at high temperature probably enables
634 a larger addition of Pb^{2+} in brannerite, but this cannot explain the local Pb enrichment
635 (*e.g.* more than 10000 ppm at Montchemin; Fig. 10f). Radiogenic Pb produced by decay of
636 U and Th, can be present in significant concentration in old brannerite, like Hidden Valley
637 and Crocker's Well (Fig. 10f). Significant lead loss has also been reported, which makes
638 geochronological data interpretation even more challenging (Lumpkin *et al*., 2012).
639 Furthermore, the common association of brannerite with galena at various scales (Figs. 3,
640 5, 6) also questions the origin of the measured Pb. Lead is a network modifier and thus,
641 as brannerite becomes metamict with time, lead is often trapped in nanometric galena
642 (Fig. 5; Lumpkin et al. 2012). Furthermore, Macmillan *et al*. (2017) suggest that galena
643 can also be (1) cogenetic with brannerite; (2) a product of the recrystallization of early
644 Pb-rich brannerite; (3) a product of uraninite dissolution. The issue of U loss in altered
645 domain (Fig. 8) and the presence of exsolution of U-rich nanodomains (Fig. 5a-c) in
646 brannerite, are also of primary importance for geochronological purposes. Accurate
647 interpretation of ages, obtained either by bulk (ID-TIMS) or high resolution in-situ
648 techniques (SIMS, LA-ICPMS) requires the petrogenesis and chemistry of both brannerite
649 and associated phases, from the microscale down to the nanoscale to be determined.
650
651 *Recovery of U and other elements from natural brannerite*

While brannerite has been explored as a matrix storage for nuclear wastes (*e.g.* Lumpkin, 2001), its refractory nature to leaching has been recently challenged in order to evaluate potential uranium recovery (*e.g.* Lottering *et al*., 2008, Charalambous *et al*., 2014; Gilligan and Nikoloski, 2015a,b). Based on tests made on natural and synthetic crystals, these authors have shown that several parameters can influence the recovery rates such as temperature, pH, and Fe^{3+} concentrations in the solvents. This last parameter is very important, as the amount of extracted U from brannerite is proportional to the Fe^{3+} concentration (Gogoleva *et al*., 2012; Charalambous *et al*., 2013, 2014). Iron substitutes for titanium in the B site and its abundance, which varies between samples, depends on the genetic types of brannerite (Figs. 11b, 12c). The high Fe content of some pegmatitic occurrences (Namibia) makes them good candidates for naturally magnifying U recovery. However, these ores are generally complex and brannerite also contains other elements such as Ca, REE and Si (Fig. 12a). While leaching mechanisms remain unknown, it appears that when uranium is partially replaced in the brannerite structure by other elements (Ce, Ca…), the extraction of uranium is reduced (Charalambous *et al*., 2010). Hence, several elements that could represent economically interesting co-products (*e.g.* REE) may also represent a limit for acceptable recovery rates of uranium from brannerite

Conclusion

Based on original analytical data from a variety of brannerite occurrences, this study demonstrates that chemical contents and REE abundances of brannerite reflect the geological conditions of their formation. Combining both results, it is possible to obtain a reliable geochemical classification at the scale of ore locality and genetic types. Such

677 fingerprints are useful for forensic science, the exploration industry, understanding
678 metallogenic process and optimizing extraction of uranium. Our dataset is not exhaustive
679 though, and it is necessary to complement it with other occurrences from other genetic
680 environments, such as uraniferous conglomerates (e.g. Elliot lake, Witwatersrand) or
681 metamorphic domains (Domes Region in Zambia). Applying our approach also requires
682 not only blind spot analyses, but a careful preliminary study or ore petrography, as
683 brannerite ores can be polyphase and chemically complex.

684 This study also points out the partial misunderstanding of various geochemical
685 processes at the atomic scale. One of the major points is the valence state of U, its origin
686 (*e.g*. the role of redox conditions for brannerite formation) and the major consequences
687 for the present complex mineral chemistry of brannerite. Itself, the presence of uranium
688 has severe effects on brannerite crystal structure and the metamict aspect of variously
689 aged natural brannerite was demonstrated (*e.g.* Lumpkin *et al*., 2012). This may be
690 responsible for the origin of various crystal defects, which may represent possible non-
691 stoichiometric traps for a variety of elements (*e.g.* Si). How to reconcile such
692 crystallographic self-alteration with the apparent pristine mineral geochemistry is not
693 therefore straightforward. Further study on natural brannerite is required to follow this
694 holistic approach and to combine various scale observation and techniques, in order to
695 meet such a challenge.

696

697 **Acknowledgements**

698

699 This article was part of the UTILE multi-disciplinary project and was sponsored by the
700 NEEDS (CNRS-AREVA-CEA) program. We greatly thank Olivier Rouer (GeoRessources,
701 Nancy), Martin Robyr (Univ Lausanne), Philippe de Parseval (centre de

microcaratérisation Raimond Castaing, Toulouse) for EPMA analyses and mapping and Nadia Guignard (IC2MP, Poitiers) for Raman spectrometry. We express our gratitude to Lubos Vrtiska (Narodni Museum, Prag), Michel Cuney (GeoRessources), Jean-Claude Leydet and Marc Brouand (Orano) for providing a part of the samples. We thank Roger Mitchell and Jason Harvey for handling the manuscript and three anonymous rewievers for their constructive comments, which helped to significantly improve the manuscript.

References

Ansermet, S. (2001) *Le Mont Chemin*. Nouvelles Imprimeries Pillet, Martigny, Suisse, 302 pp.

Ashley, P.M. (1984) Sodic granitoids and felsic gneisses associated with uranium-thorium mineralisation, Crockers Well, South Australia. *Mineralium Deposita*, **19**, 7-18.

Azor, A., Ballèvre, M. (1997) Low-Pressure Metamorphism in the Sierra Albarrana Area (Variscan Belt, Iberian Massif). *Journal of Petrology*, **38**, 35-64.

Barféty, J.-C., Bordet, P., Carme, F., Debelmas, J., Meloux, M., Montjuvent, G., Mouterde, R., Sarrot-Reynauld, J. (1972). Carte géologique détaillée de la France à 1/50.000°, feuille Vizille, *BRGM*, Geological Map.

Belissont, R., Boiron, M.-C., Luais, B. Cathelineau, M. (2014) LA-ICP-MS analyses of minor and trace elements and bulk Ge isotopes in zoned Ge-rich sphalerites from the Noailhac–Saint-Salvy deposit (France): Insights into incorporation mechanisms and ore deposition processes. *Geochimica Cosmochimica Acta*, **126**, 518–540.

Bianconi, F., Simonetti, A. (1967) La brannerite e la sua paragenesis nelle pegmatite di Lodrino (Ct. Ticino). *Schweizerische Mineralogische und Petrographische Mitteilungen*, 47, 887–934.

727 Bonne, M., Pronier, S., Batonneau, Y., Can, F., Courtois, X., Royer, S., Marécot, P., Duprez, P.
728 (2010) Surface properties and thermal stability of SiO_2-crystalline TiO_2 nano-
729 composites. *Journal of Materials Chemistry*, **20**, 9205. DOI: 10.1039/c0jm01184c.
730 Branche G., Chervet J., Guillemin C. (1952) Nouvelles espèces uranifères françaises. CEA,
731 Report, 128.
732 Burri, T., Berger, A., Engi, M. (2005) Tertiary migmatites in the Central Alps: Regional
733 distribution, field relations, conditions of formation, and tectonic implications.
734 *Schweizerische Mineralogische und Petrographische Mitteilungen*, **85**, 215-232.
735 Campana, B., King, D. (1958). Regional geology and mineral resources of the Olary
736 province. *Geological Survey of South Australia Bulletin*, **30**, 7–50.
737 Charalambous, F.A. (2013) *Synthesis, characterisation and dissolution of brannerite. A*
738 *Uranium Titanate Mineral.* PhD Dissertation, RMIT University, Melbourne, Australia.
739 Charalambous, F.A., Ram, R., McMaster, S., Pownceby, M.I., Tardio, J., Bhargava, S.K. (2014)
740 Leaching behaviour of natural and heat treated brannerite-containing uranium ores in
741 sulphate solutions with iron (III). *Minerals Engineering*, **57**, 25–35.
742 Charalambous, F.A., Ram, R.,McMaster, S., Tardio, J., Bhargava, S.K. (2013) An investigation
743 on the dissolution of synthetic brannerite (UTi2O6). *Hydrometallurgy*, **139**, 1–8.
744 Charalambous, F.A., Ram, R., Pownceby, M.I., Tardio, J., Bhargava, S.K. (2012) Chemical and
745 microstructural characterisation studies on natural and heat treated brannerite
746 samples. *Minerals Engineering*, **39**, 276–288.
747 Charalambous, F.A., Ram, R., Tardio, J., Bhargava, S.K. (2010) Characterisation and
748 dissolution studies on various forms of brannerite. Pp. p597–p608 in: *Proceedings of*
749 *the Third International Conference on Uranium, 40th Annual Hydrometallurgy Meeting*,
750 Saskatoon, Canada, August 2010.

751 Coats, R.P., Blissett, A.H. (1971) Regional and Economic Geology of the Mount Painter
752 Province. Geological Survey of South Australia Bulletin, Vol. 43, Adelaide, 426 pp.
753 Colella, M., Lumpkin, G.R., Zhang, Z., Buck, E.C., Smith, K.L. (2005) Determination of the
754 uranium valence state in the brannerite structure using EELS, XPS, and EDX. *Physics*
755 *and Chemistry of Minerals*, **32**, 52–64.
756 Contreras M.C., Garrote A., Sánchez-Carretero, R. (1983) Pegmatitas en materiales
757 metamórficos del norte de la provincia de Córdoba: mineralogía y posibilidades
758 económicas. *Cuad Lab Xeol Laxe*, **6**, 415–428.
759 Copeland, P., Harrison, T.M., Hodges, K.V., Maruéjol, P., Lefort, P. and Pecher, A. (1991) An
760 early pliocène thermal disturbance of the main central thrust, central Nepal:
761 Implications for Himalayan tectonics. *Journal of Geophysical Research*, **96**, 8475-8500.
762 Cuney, M., Friedrich, M. (1987) Physicochemical and crystal-chemical controls on
763 accessory mineral paragenesis in granitoids: implications for uranium metallogenesis.
764 *Bulletin de Minéralogie*, **110**, 235–247.
765 Cuney, M. (2010) Evolution of uranium fractionation processes through time: driving the
766 secular variation of uranium deposit types. *Economic Geology*, **105**, 553–569.
767 Dallmeyer R.D., Quesada, C. (1992) Cadomian vs. variscan evolution of the Ossa Morena
768 Zone (SW Iberia): field and 40Ar/30Ar mineral age constraints. *Tectonophysics*, **216**,
769 339-364.
770 Ditz, R., Sarbas, B., Schubert, P., Töpper, W. (1990) *Th Thorium - Natural Occurrence.*
771 *Minerals (Excluding Silicates)*. Springer-Verlag Berlin, Heidelberg, 392 pp.
772 Duran, C.J., Seydoux-Guillaume, A.-M., Bingen, B., Gouy, S., de Parseval, P., Ingrin, J.,
773 Guillaume, D. (2016) Fluid-mediated alteration of (Y,REE,U,Th)–(Nb,Ta,Ti) oxide
774 minerals in granitic pegmatite from the Evje-Iveland district, southern Norway.
775 *Mineralogy and Petrology*, **110**, 581-599.

776 Eglinger, A., André-Mayer, A.-S., Vanderhaeghe, O., Mercadier, J., Cuney, M., Decrée, S.,
777 Feybesse, J.-L., Milesi, J.-P. (2013) Geochemical signatures of uranium oxides in the
778 Lufilian belt: from unconformity-related to syn-metamorphic uranium deposits during
779 the Pan-African orogenic cycle. *Ore Geology Reviews*, **54**, 197–213.
780 Ennaciri, A. (1995) *Contribution a l'étude du district a Co, As, (Ni, Au, Ag) de Bou Azzer, Anti*
781 *Atlas (Maroc), données mineralogiques et geochimiques; étude des inclusions fluids*. PhD
782 dissertation, Université d'Orléans, France.
783 Ennaciri, A., Barbanson, L., and Touray, J.-C. (1997) Brine inclusions from the Co-As(Au)
784 Bou Azzer district, Anti-Atlas Mountains, Morocco. *Economic Geology*, **92**, 360–367.
785 Finnie, K.S., Zhang, Z., Vance, E.R., Carter, M.L. (2003) Examination of U valence states in
786 the brannerite structure by near-infrared diffuse reflectance and X-ray photoelectron
787 spectroscopies. *Journal of Nuclear Materials*, 317, 46–53.
788 Foden, J., Elburg, M.A., Dougherty-Page, J., Burtt, A. (2006) The timing and duration of the
789 Delamerian Orogeny: correlation with the Ross Orogen and implications for Gondwana
790 Assembly. *Journal of Geology,* **114**, 189–210.
791 Förster, H.-J. (1999) The chemical composition of uraninite in Varsican granites of the
792 Erzgebirge, Germany. *Mineralogical Magazine*, **63**, 239–252.
793 Frimmel, H.E., Schedel, S., Brätz, H. (2014) Uraninite chemistry as forensic tool for
794 provenance analysis. *Applied Geochemistry*, **48**, 104–121.
795 Garotte, A., Ortega Huertas, M., Romero, J. (1980) Los yacimentos de pegmatitas de Sierra
796 Albarrana (Provincia de Cordoba, Sierra Morena) Pp. 145-168 in *1a Reunion sobre la*
797 *geologia de Ossa-Morena*. Temas Geologica Minros, Madrid, Spain.
798 Gasquet, D., Bertrand, J.-M., Paquette, J.-L., Lehmann, J., Ratzov, G., Guedes, R.A., Tiepolo,
799 M., Boullier, A.-M., Scaillet, S., Nomade, S. (2010) Miocene to Messinian deformation and
800 hydrothermal activity in a pre-Alpine basement massif of the French western Alps: new

U–Th–Pb and argon ages from the Lauzière massif. *Bulletin de la Société Géologique de France*, **181**, 227–241.

Geffroy, J. (1963) La brannerite du filon aurifere de la Gardette (Isere) et sa signification metallogenique. *Bulletin de la Société de France de Minéralogie et Cristallographie*, **86**, 129–132.

Gilligan, R., Nikoloski, A.N. (2015a). The extraction of uranium from brannerite — a literature review. *Minerals Engineering*, **71**, 34–48.

Gilligan, R., Nikoloski, A.N. (2015b). Leaching of brannerite in the ferric sulphate system. Part 1: kinetics and reaction mechanism. *Hydrometallurgy*, **156**, 71–80.

Giuliani, G., France-Lanord, C., Coget, P., Schwarz, D., Cheilletz, A., Branquet, Y., Giard, D., Pavel, A., Martin-Izard, A., Piat, D.H. (1998) Oxygen isotope systematic of emerald: relevance for its origin and geological significance. *Mineralium Deposita*, **33**, 513–519.

Giuliani, G., Fallick, A.E., Garnier, V., France-Lanord, C., Ohnenstetter, D., Schwarz, D. (2005) Oxygen isotope composition as a tracer for the origins of rubies and sapphires. *Geology*, **33**, 249–252.

Gogoleva, E.M. (2012) The leaching kinetics of brannerite ore in sulfate solutions with iron(III). *Journal of Radioanalytical and Nuclear Chemistry*, **293**, 185–191.

Goldney, L.H., Canning, R.G., Gooden, J.E.A. (1972) Extraction Investigations with Some Australian Uranium Ores. Pp 1-18 in: A*AEC Symposium on Uranium Processing*, Australian Atomic Energy Commission: Adelaide, Australia.

González del Tánago, J., Arenas, R. (1991) Amfibolitas graatiferas de Sierra Albarrana (Cordoba). Termobarometria e implicaciones para el desarrollo del metamorfismo regional. *Revista de la Sociedad Geologica de Espana*, **4**, 251-269.

Goscombe, B.D., Hand, M., Gray, D., Mawby, J. (2003) The metamorphic architecture of a transpressional orogen: the Kaoko Belt, Namibia. *Journal of Petrology*, **44**, 676–711.

826 Goscombe, B., Gray, D., Armstrong, R., Foster, D.A., Vogl, J. (2005) Event geochronology of
827 the Pan-African Kaoko Belt, Namibia. *Precambrian Research*, **140**, 103.e1–103e41.
828 Graeser, S., Guggenheim, R. (1990) Brannerite from Lengenbach, Binntal (Switzerland).
829 *Schweizerische Mineralogische und Petrographische Mitteilungen*, **70**, 325–331.
830 Guastoni, A., Pennacchioni G., Pozzi G., Fioretti, A.M., Walter J.M. (2014) Tertiary
831 pegmatite dikes of the Central Alps. *The Canadian Mineralogist*, **52**, 191-219.
832 Hewett, D.F., Stone, J., Levine, H. (1957). Brannerite from San Bernardino County,
833 California. *American Mineralogist*, **42**, 30–38.
834 Kissin, S.A. (1992) Five-element (Ni–Co–As–Ag–Bi) veins. *Geoscience Canada*, **19**, 113–
835 124.
836 Koch I. (2012) *Analysis of multivariate and high-dimensional data theory and practice*.
837 Cambridge University Press, Cambridge, 504 pp.
838 Kröner, A., Rojas-Agramonte, Y. (2017) Mesoproterozoic (Grenville-age) granitoids and
839 supracrustal rocks in Kaokoland, northwestern Namibia, *Precambrian Research*, **98**,
840 572-592.
841 Kröner, A., Rojas-Agramonte, Y., Hegner, E., Hoffmann, K.-H., Wingate, M.T.D. (2010)
842 SHRIMP zircon dating and Nd isotope systematics of Palaeoproterozoic migmatitic
843 orthogneisses in the Epupa Metamorphic Complex of NW Namibia. *Precambrian*
844 *Research*, **183**, 50–69.
845 Lê, S., Josse, J. & Husson, F. (2008) FactoMineR: An R Package for Multivariate Analysis.
846 *Journal of Statistical Software*, 25. 1-18.
847 Leblanc, M., Billaud, P. (1982) Cobalt arsenide ore bodies related to an upper Proterozoic
848 ophiolite; Bou Azzer (Morocco). *Economic Geology*, **77**, 162–175.

849 Leblanc, M., Lbouabi, M. (1988) Native silver mineralization along a rodingite tectonic
850 contact between serpentinite and quartz diorite (Bou Azzer, Morocco). *Economic*
851 *Geology*, **83**, 1379-1391.
852 Leblanc M. (1986) Co-Ni arsenide deposist with accessory gold, in ultramafic rocks from
853 Morocco. *Canadian Journal of Earth Science*, **23**, 1592-1602.
854 Longerich H.P., Jackson S.E. and Gunther D. (1996) Laser ablation inductively coupled
855 plasma mass spectrometric transient signal data acquisition and analyte concentration
856 calculation. *Journal of Analytical Atomic Spectrometry*, **11**, 899–904.
857 Lottering, M.J., Lorenzen, L., Phala, N.S., Smit, J.T., Schalkwyk, G.A.C. (2008). Mineralogy
858 and uranium leaching response of low grade South African ores. *Minerals Engineering,*
859 **21**, 16–22.
860 Ludwig, K.R., Cooper, J.A. (1984) Geochronology of Precambrian granites and associated
861 U–Ti–Th mineralization, northern Olary province, South Australia. *Contributions to*
862 *Mineralogy and Petrology*, **86**, 298–308.
863 Lumpkin, G.R. (2001). Alpha-decay damage and aqueous durability of actinide host
864 phases in natural systems. *Journal of Nuclear Materials*, **289**, 136-166.
865 Lumpkin, G.R., Leung, S.H.F., Ferenczy, J. (2012) Chemistry, microstructure, and alpha
866 decay damage of natural brannerite. *Chemical Geology*, **291**, 55–68.
867 Machault, J., Barbanson, L., Augé, T., Bailly, L., Orgeval, J.-J. (2014) Mineralogical and
868 microtextural parameters in metals ores traceability studies. *Ore Geology Reviews*, **63**,
869 307-327.
870 Macmillan, E., Cook, N.J., Ehrig, K., Pring, A. (2017) Chemical and textural interpretation of
871 late-stage coffinite and brannerite from the Olympic Dam IOCG-Ag-U deposit,
872 *Mineralogical Magazine*, **81**, 1323–1366.

873 Marshall, D., Meisser, N., Taylor, R.P. (1998) Fluid inclusion, stable isotope and Ar-Ar
874 evidence for the age and origin of gold-bearing quartz veins at Mont Chemin,
875 Switzerland, *Mineralogy and Petrology*, **62**, 147–165.
876 Marudjol, P. (1988) *Métasomatose alcaline et mindralisations uranifères: les albitites du*
877 *gisement de Lagoa Real (Bahia, Brésil) et exemples complémentaires de Xihuashan (SE*
878 *Chine), Zheltorechensk (Ukraine) et Chhuling Khola (Népal central).* PhD dissertation,
879 Insitut National Polytechnique de Lorraine, Nancy.
880 Mcdonough, W.F., Sun, S.S. (1995) The composition of the earth. *Chemical Geology*, **120**,
881 223–253.
882 Meisser, N. (1998) La géologie et les concentrations minérales du Mont Chemin. *Minaria*
883 *Helvetica*, **18b**, 66-82.
884 Melcher, F., Sitnikova, M.A., Graupner, T., Martin, N., Oberthür, T., Henjes-Kunst, F., Gäbler,
885 H.-E., Gerdes, A., Brätz, H., Davis, D.W., Dewaele, S. (2008) Fingerprinting of conflict
886 minerals: columbite–tantalite ("coltan") ores. *SGA News*, **23**, 6–14.
887 Melcher, F., Graupner, T., Gäbler, H.-E., Sitnikova, M.A., Henjes-Kunst, F., Oberthür, T.,
888 Gerdes, A., Dewaele, S. (2015) Tantalum–(niobium–tin) mineralisation in African
889 pegmatites and rare metal granites: constraints from Ta-Nb oxide mineralogy,
890 geochemistry and U–Pb geochronology. *Ore Geology Reviews*, **64**, 667-719.
891 Mercadier, J., Cuney, M., Lach, P., Boiron, M.-C., Bonhoure, J., Richard, A., Leisen, M., Kister,
892 P. (2011) Origin of uranium deposits revealed by their rare earth element signature.
893 *Terra Nova*, **23**, 264–269.
894 Mesbah, A., Szenknect, S., Clavier, N., Lin, H., Baron, F., Beaufort, D., Batonneau, Y.,
895 Mercadier, J., Eglinger, A., Turuani, M., Goncalves, P., Choulet, F., Chapon, V., Seydoux-
896 Guillaume, A.-M., Pagel, M., Dacheux, N. (2019) Direct synthesis of pure brannerite
897 UTi_2O_6, *Journal of Nuclear Materials*, **515**, 401-406.

898 Mysen, B.O., Richet, P. (2005) *Silicate Glasses and Melts: Properties and Structure*. Elsevier,
899 Amsterdam, 555 pp.
900 Oberthür, T., Melcher, F., Henjes-Kunst, F., Gerdes, A., Stein, H., Zimmerman, A., El Ghorfi,
901 M. (2009) Hercynian age of the cobalt-nickel-arsenide-(gold) ores, Bou Azzer, Anti
902 Atlas, Morocco: Re–Os, Sm–Nd, and U–Pb age determinations. *Economic Geology*, **104**,
903 1065–1079.
904 Pagel, M., Pinte, G., Rotach-Toulhoat, N. (1987) The rare earth elements in natural
905 uranium oxides. *Monograph Series on Mineral Deposits*, **27**, 81–85.
906 Pajo, L., Mayer, K., Koch, L. (2001) Investigation of the oxygen isotopic composition in
907 oxidic uranium compounds as a new property in nuclear forensic science. *Fresenius*
908 *Journal of Analytical Chemistry*, **371**, 348–352.
909 Patchett, J.E., Nuffield, E.W. (1960) Studies of radioactive compounds: X-The synthesis of
910 crystallography of brannerite. *The Canadian Mineralogist*, **6**, 483-490.
911 Paton, C., Hellstrom, J., Paul, B., Woodhead, J., Hergt, J. (2011) Iolite: Freeware for the
912 visualisation and processing of mass spectrometric data. *Journal of Analytical Atomic*
913 *Spectrometry*, **26**, 2508–2518.
914 Pearce N.J.G., Perkins W.T., Westgate J.A., Gorton M.P., Jackson S.E., Neal C.R., Chenery S.P.
915 (1997) A compilation of new and published major and trace element data for NIST SRM
916 610 and NIST SRM 612 glass reference materials. *Geostandards and Geoanalytical*
917 *Research*, **21**, 115-144.
918 Pêcher, A. (1989) The metamorphism in the Central Himalaya. *Journal of Metamorphic*
919 *Geology*, **7**, 31-41.
920 Pointeau, V., Deditius, A., Miserque, F., Renock, D., Becker, U., Zhang, J., Clavier, N., Dacheux,
921 N., Poinssot, C., Ewing, R. (2009) Synthesis and characterization of coffinite. *Journal of*
922 *Nuclear Materials*, **393**, 449-458.

923 Polito, P.A., Kyser, T.K., Stanley, C. (2009) The Proterozoic, albitite-hosted, Valhalla
924 uranium deposit, Queensland, Australia: a description of the alteration assemblage
925 associated with uranium mineralisation in diamond drill hole V39. *Mineralium*
926 *Deposita*, **44**, 11–40.
927 Press, W.H., Flannery, B.P., Teukolsky, S. A., Vetterling, W.T. (1986) *Numerical Recipes, The*
928 *Art of Scientific Computing*. Cambridge University Press, Cambridge, 818 pp.
929 Purdy, J.W., Stalder, H.A. (1973): K-Ar Ages of Fissure Minerals from the Swiss Alps.
930 *Schweizerische Mineralogische und Petrographische Mitteilungen*, **53**, 79-98.
931 René, M., Dolníček, Z. (2017) Uraninite, Coffinite and Brannerite from Shear-Zone Hosted
932 Uranium Deposits of the Bohemian Massif (Central European Variscan Belt). Minerals,
933 7, 50. doi: 10.3390/min7040050.
934 Rojkovic, I., Boronikhin, V.A. (1982) U-Ti minerals at the deposit Novoveska Huta
935 (Slovenske Rudohorie Mts.). *Geologicky Zbornik*, **33**, 321-330.
936 Rojkovic, I., Novotny, L., Haber, M. (1993) Stratiform and vein U, Mo and Cu mineralization
937 in the Novoveskfi Huta area, CSFR. *Mineralium Deposita*, **28**, 58-65.
938 Rütti, R., Marquer, D., Thompson, A.B. (2008) Tertiary tectono-metamorphic evolution of
939 the European margin during Alpine collison: example of the Leventina Nappe (Central
940 Alps, Switzerland), *Swiss Journal of Geosciences*, **101**, S157–S171.
941 Sapsford, D.J., Bowell, R.J., Geroni, J.N., Penman, K.M., Dey, M. (2012) Factors influencing
942 the release rate of uranium, thorium, yttrium and rare earth elements from a low grade
943 ore. *Minerals Engineering*, **39**, 165–172.
944 Seydoux-Guillaume, A.-M., Bingen, B., Paquette, J.-L., Bosse, V. (2015) Nanoscale evidence
945 for uranium mobility in zircon and the discordance of U-Pb chronometers. *Earth and*
946 *Planetary Science Letters*, **409**, 43–48.

947 Shannon R.D. (1976) Revised effective ionic radii and systematic studies of interatomic
948 distances in halides and chalcogenides. *Acta Crystallographica*, **32**, 751-767.
949 Smith, D.K. Jr. (1984) Uranium mineralogy. Pp. 43-88 in: *Uranium Geochemistry,*
950 *Mineralogy, Geology, Exploration and Resources* (B. de Vivo, F. Ippolito, G. Capaldi, P.R.
951 Simpson, editors). The Institution of Mining and Metallurgy, London.
952 Spano, T.L., Simonetti, A., Balboni, E., Dorais, C., Burns P.C. (2017) Trace element and U
953 isotope analysis of uraninite and ore concentrate: applications for nuclear forensic
954 investigations. *Applied Geochemistry*, **84** (Suppl. C), 277–285.
955 Števko, M., Uher, P., Ondrejka, M., Ozdín, D, Bačík, P. (2014) Quartz–apatite–REE
956 phosphates–uraninite vein mineralization near Čučma (eastern Slovakia): a product of
957 early Alpine hydrothermal activity in the Gemeric Superunit, Western Carpathians.
958 *Journal of Geosciences*, **59**, 209–222.
959 Szymanski, J.T., Scott, J.D. (1982) A crystal structure refinement of synthetic brannerite,
960 UTi_2O_6, and its bearing on rate of alkaline-carbonate leaching of brannerite in ore. *The*
961 *Canadian Mineralogist*, **20**, 271–279.
962 Vance, E.R., Watson, J.N., Carter, M.L., Day, R.A., Lumpkin, G.R., Hart, K.P., Zhang, Y.,
963 McGlinn, P.J., Stewart, M.W.A., Cassidy, D.J. (2000). Crystal chemistry, radiation effects
964 and aqueous leaching of brannerite, UTi_2O_6. *Ceramic Transactions*, **107**, 561–568.
965 Vance, E.R., Watson, J.N., Carter, M.L., Day, R.A., Begg, B.D. (2001) Crystal chemistry and
966 stabilization in air of brannerite, UTi_2O_6. *Journal of the American Ceramic Society*, **84**,
967 141–144.
968 Vozárová, A., Šarinová, K., Sergeev, S., Larionov, A., Presnyakov, S. (2010) Late
969 Cambrian/Ordovician magmatic arc type volcanism in the Southern Gemericum
970 basement, Western Carpathians, Slovakia: U–Pb (SHRIMP) data from zircons.
971 *International Journal of Earth Sciences*, **99**, 17–37.

Vozárová, A., Konecný, P., Šarinová, K., Vozár, J. (2014) Ordovician and Cretaceous tectonothermal history of the Southern Gemericum Unit from microprobe monazite geochronology (Western Carpathians, Slovakia). *International Journal of Earth Sciences*, **103**, 1005–1022.

Wenk, E. (1970) Zur Regionalmetamorphose und Ultrametamorphose im Lepontin. *Fortschritte der Mineralogie*, **47**, 34–51.

Wilde, A., Otto, A., Jory, J., MacRae, C., Pownceby, M., Wilson, N., Torpy, A. (2013) Geology and Mineralogy of Uranium Deposits from Mount Isa, Australia: Implications for Albitite Uranium Deposit Model. *Minerals*, **3**, 258-283.

Wülser, P.-A. (2009) *Uranium metallogeny in the North Flinders Ranges region of South Australia*. PhD dissertation, Adelaide University, Australia.

Zhang, Y.J., Karatchevtseva, I., Qin, M.J., Middleburgh, S.C., Lumpkin, G.R. (2013) Raman spectroscopic study of natural and synthetic brannerite, *Journal of Nuclear Materials*, **437**, 149-153.

Zhang, Y.J., Lumpkin, G.R., Li, H., Blackford, M.G., Colella, M., Carter, M.L., Vance, E.R. (2006) Recrystallization of amorphous natural brannerite through annealing: the effect of radiation damage on the chemical durability of brannerite. *Journal of Nuclear Materials*, **350**, 293–300.

Figure captions

FIG. 1. Crystal structure of Brannerite, down the b axis (modified after Mesbah *et al*., 2019).

FIG. 2. Map showing the location of studied brannerite sample and their genetic type.

FIG. 3. Back-Scattered Scanning Electron (BSE) images of studied hydrothermal brannerite: *(a)* brannerite from La Gardette, associated with Cu-Bi sulphides and surrounded by a corroded grain boundary; *(b)* altered (upper right corner) and unaltered brannerite from Bou Azzer. The location of Focused Ion Beam (FIB) foil cut across unaltered brannerite is reported; *(c)* detailed view of altered Bou Azzer brannerite characterized by a complex association U-rich and U-poor domains. Note the presence of radial fractures filled with coffinite around altered brannerite; *(d)* stockwork with early brannerite (Br I) crosscut by two successive brannerite veins (Br II and Br III) from Himalaya; *(e)* partly altered (light grey) brannerite crystal from Mont Chemin; *(f)* brannerite from Kratka wValley, associated with undetermined Ti oxides and minute uraninite inclusions. The location of Raman analyses (R) is reported for each brannerite sample. Abbreviations: Ab: Albite; Ang: Anglesite; Brn: Brannerite; Cer: Cerussite; Cof: Coffinite; Gn: Galena; Qz: Quartz; Urn: Uraninite.

FIG. 4. *(a)* to *(d)* qualitative EDS-SEM X-ray chemical maps of brannerite crystals from Bou Azzer occurrence; *(e)* to *(h)* quantitative FE-EPMA element distribution maps from Himalaya occurrence.

FIG. 5. Transmission Electron Microscope (TEM) and Scanning TEM (STEM) images from a FIB foil cut across a brannerite crystal from Bou Azzer: *(a)* TEM Bright Feld (BF) image showing the abundance of U-rich and more rarely Pb-rich inclusion within brannerite (Brn). Inset corresponds to Selective Area Electron Diffraction (SAED) pattern from

1018 brannerite full with U-rich inclusionsand demonstrates its amorphous state; *(b)* STEM
1019 HAADF (High Angle Annular Dark Field) (STEM-DF) image of a zoom from area shown in
1020 A. In this mode, bright areas correspond to high density materials (*e.g.* U-rich or Pb-rich
1021 inclusion) or thicker regions. The white rectangle indicates location of EDS chemical
1022 maps; *(c)* to *(e)* U, Ti and Pb chemical maps from the same area, revealing the presence of
1023 Pb and U-rich domains;
1024 FIG. 6. Back-Scattered Scanning Electron (BSE) images of studied pegmatitic brannerite;
1025 *(a)* brannerite monocrystal from Crocker's Well, showing pervasive cracking and
1026 chemical zoning due to variable Th enrichment; *(b)* brannerite from Hidden Valley
1027 exhibiting altered domains along fracture (dark grey), uraninite inclusions and a complex
1028 corroded boundary; *(c)* brannerite from El Cabril with uraninite inclusions and pervasive
1029 corrosion along grain margins; *(d)* brannerite from El Cabril showing partial replacement
1030 by secondary uraninite, Ti oxide and unknown Y-rich minerals (see Fig. 6d); *(e)* partly
1031 altered brannerite from Lodrino pegmatite. The location of Focused Ion Beam (FIB) foil
1032 cut across unaltered brannerite is reported; (*f*) secondary uranium minerals developing
1033 along cracks in brannerite from NA12 pegmatite (Namibia). The location of Raman
1034 analyses (R) is reported for each brannerite sample. Abbreviations: Brn: Brannerite; Cof:
1035 Coffinite; Kfs: K-feldspar; Urn: Uraninite.
1036 FIG. 7. Quantitative FE-EPMA element distribution maps from El Cabril occurrence.
1037 FIG. 8. Transmission Electron Microscope (TEM) and Scanning TEM (STEM) images from
1038 a FIB foil cut across a brannerite crystal from Lodrino (*a* to *e*): *(a)* TEM-BF image, showing
1039 the presence of altered domains within unaltered brannerite. Selected Area Electron
1040 Diffraction (SAED) patterns from unaltered brannerite (inset in the top) also supports the
1041 amorphous state of brannerite, while SAED pattern from altered brannerite (inset in the
1042 bottom) indicate the presence of nanocrystalline domains (possibly coffinite); *(b)* STEM-

1043 DF image of a zoom in the same area; *(c)* to *(e)* U, Ti and Si chemical maps from the same
1044 area, demonstrating depletion or enrichment in the altered domain relative to the
1045 unaltered domain. Brn: brannerite.
1046 FIG. 9. Boxplots of major and minor element contents for each studied brannerite sample,
1047 considering its genetic type. Contents are given in apfu calculated on a basis of 6 oxygen
1048 atoms from EPMA results (Table 1). For Y, abundances obtained by LA-ICPMS
1049 measurement and available in Table 2 are reported. Dashed line represents the
1050 theoretical U and Ti contents of ideal UTi_2O_6 brannerite.
1051 FIG. 10. Boxplots of trace element abundance measured by LA-ICPMS for each studied
1052 brannerite sample, considering the hydrothermal (blue) and pegmatitic (red) genetic
1053 types.
1054 FIG. 11. Principal component analysis of the EPMA dataset of major and minor element
1055 contents in brannerite from diverse genetic types. Left frames: spot analyses (*i.e.*
1056 individuals) plotted on the PC1 (Dim1) vs. PC2 (Dim2) plane, with respective percentage
1057 that explain the element content variability. Right frames: elements (*i.e.* variables) plotted
1058 in the same plane.
1059 FIG. 12. Binary diagrams of selected A site cations versus calculated U^{4+} content *(a)* to *(c)*
1060 and average U valence *(d)* to *(f)* of brannerite in atoms per formula unit (apfu). Details for
1061 calculation of U^{4+} content and average U valence are provided in the material and methods
1062 section, following Collela *et al*. (2005). Since only Y and Ce were measured by EPMA, it is
1063 not possible to draw a trend curve for substitution (4).
1064 FIG. 13. Binary diagram of selected B site cations versus Ti content *(a)* and average U
1065 valence of brannerite *(b)* in atoms per formula unit (apfu).
1066 FIG. 14. Binary and ternary plots, illustrating the substitution rates at sites A and B and
1067 the relative proportions of substituents: *(a)* Ternary plot, including Si abundance and

showing discernible substitution type and rate depending on brannerite genetic types; *(b)* Ternary plot showing the relative proportion of each major A site substituents and *(c)* Fe versus Al content in brannerite, showing various occupancy of B site (excluding Ti) depending on genetic type and redox conditions.

FIG. 15. Synoptic chart illustrating the results of two-sample Kolmogorov-Smironoff test. For each element, its distribution was compared between two samples (locality or genetic type). The more red coloured cases there are, the more significant differences in mineral chemistry between samples there are.

FIG. 16. Chondrite-normalized REE patterns from brannerite *(a)* to *(b)* and associated uranium phases *(c)* from hydrothermal and pegmatitic types. Normalisation values are from McDonough and Sun (1995).

FIG. 17. Total REE versus chondrite normalised light over heavy REE for brannerite of hydrothermal and pegmatitic types. Normalisation values are from McDonough and Sun (1995).

TABLE 1. Compositional data from EPMA analyses for brannerite of hydrothermal, and magmatic genetic types. * Fe_2O_3 recalculated from FeO. SD: Standard deviation. n.d.: not detected. SD: Standard Deviation.

TABLE 2. Trace Element data from LA-ICPMS analyses for brannerite of hydrothermal, and magmatic genetic types. (ΣLREE)N = LaN+CeN+PrN+NdN+SmN; (ΣHREE)N = ErN+TmN+YbN+LuN."N for chondrite-normalised. n.d.: not detected. SD: Standard Deviation.

1093 Appendix - Geological setting of studied brannerite samples

1094

1095 *Geological setting of hydrothermal brannerite*

1096

1097 La Gardette Mine (GD) is located in Western French Alps close to Bourg-d'Oisans
1098 city. Alpine-type quartz veins crosscut the amphibolite of the Variscan basement and its
1099 Triassic carbonate cover (Debelmas *et al*., 1972). Ore minerals include native gold, galena,
1100 pyrite, chalcopyrite, tennantite and brannerite (Geffroy, 1963). Age of mineralization is
1101 currently unknown but it could be related to Upper Miocene (ca. 5-11 Ma) episodes of
1102 hydrothermal fluid circulation recorded in the Belledonne Massif to the Northwest
1103 (Gasquet *et al*., 2010).

1104 The Bou Azzer (BA) deposit is located in the Moroccan Anti Atlas Belt. It occurs
1105 within a Proterozoic ophiolitic unit covered by unconformable Palaeozoic sedimentary
1106 rocks (Leblanc and Billaud, 1982). Bou Azzer is classified as a particular case of Five-
1107 Element Vein-Type deposits (Leblanc, 1986; Kissin, 1992); it is currently mined for Co Ni,
1108 Ag and Au. The polyphase mineralization includes an early Ni-Co-Fe arsenide stage
1109 followed by a late Cu-Zn-Fe sulfide stage (Ennaciri *et al*., 1997) related to high salinity
1110 brines (Leblanc and Lbouabi, 1988). While uraninite is present throughout the whole
1111 mineralization evolution, brannerite only occurs during the latest stage in association
1112 with molybdenite, chlorite, and quartz (Ennaciri, 1995). Brannerite stage has been dated
1113 by U-Pb LA-ICPMS method at 310 ± 5 Ma (Oberthür *et al*., 2009).

1114 Brannerite (HL) was collected in the Chhuling Khola Valley in Nepal. This area
1115 consists of a series of schists, gneisses, and migmatites that belong to the Greater
1116 Himalayan Sequence, which is thrusted over the low-grade metamorphic rocks of the
1117 Lesser Himalayan Sequence, along the Main Central Thrust (Pêcher, 1989). Among these

high-grade gneisses, an albitized and U-mineralized zone is exposed (Maruejol, 1988). While biotite gneisses have recorded an early sodic metasomatic stage coeval with ductile deformation along the MCT, brannerite co-precipitated with secondary albite in brittle veins forming a stockwork zone. Formation of brannerite is considered as the result of alteration of Ti oxides of the biotite gneisses by Na-U alkaline and oxidizing fluids (Maruejol, 1988) under low-grade metamorphic conditions. Isotope Dilution termal ionization mass spectrometry (ID-TIMS) U-Pb dating on brannerite has given a crystallization $^{206}Pb/^{238}U$ age at 4.8 Ma (Copeland *et al*., 1991).

The Mont Chemin (MC) mines are located in the eponymous mountain in Western Valais, Switzerland. The mines have been exploited from Middle Age until to the 20th century for Au, Ag, Pb, Fe, and fluorite (Ansermet, 2001). The veins crosscut the metamorphic Variscan basement (external crystalline massif) and particularly small late Palaeozoic granite intrusions within gneisses. At the Tête des Econduits, quartz veins include scheelite, anatase, fluorite, native Au, and brannerite (Meisser, 1998). These Alpine-type veins are probably related to a regional Miocene episode of hydrothermal fluid circulation at *ca* 10 Ma (Marshall *et al*., 1998).

The Kratka Valley (KV) occurrences are located to the north of Gemerska Poloma between Dobsina and Kosice in Eastern Slovakia. U-bearing quartz veins occur within the Ordovician Vlachovo Formation of the Southern Gemericum Unit (Vozarova *et al*., 2010). This volcano-sedimentary sequence was further intruded by Permian granites, covered by Mesozoic sediments and affected by Cretaceous regional metamorphism (Vozarova *et al*., 2014). A wide range of U mineralization is found within the Gemericum Unit, including U-Mo mineralized horizons, stratiform Cu-U redbeds and U-Mo stockworks (Rojkovic *et al*., 1993). U-Ti oxides, including brannerite, were reported from several localities (Rojkovic and Boronikhin, 1982). At Kratka Valley, brannerite-bearing quartz veins also

contain gold, arsenopyrite, chalcopyrite, molybdenite, pyrite, rutile, uraninite as well as many secondary U minerals. Timing of brannerite formation is currently unknown, but Lower Jurassic (Stevko *et al*., 2014) and Lower Cretaceous (Rojkovic *et al*., 1993) mineralizing events have been reported in the area.

Geological setting of pegmatitic brannerite

The Crocker's Well (CW) prospect, located in the southern part of Central Australia is a uranium occurrence discovered in 1951. Ore is hosted by peraluminous sodic granitoids, mainly adamellite and trondhjemite, and minor sodic gneisses (Ashley, 1984, and reference therein). Emplacement of this suite has been dated by zircon ID-TIMS (isotopic Dilution Thermal ionization Mass spectrometry) U-Pb at 1579.2 ± 1.5 Ma (Ludwig and Cooper, 1984). Although the distribution of brannerite is controlled by fractures (Campana and King, 1958), the vein systems and the mineralized breccia are restricted to the host granite, which did not experience hydrothermal alteration. Brannerite is associated with quartz, F-bearing phlogopite, sodic plagioclase, fluorapatite, niobian rutile, monazite, muscovite, chlorite, tourmaline, and fluorite (Ashley, 1984). Brannerite formation probably results from the evolution of a late peraluminous magmatic system, as indicated by the younger $^{206}Pb/^{238}U$ ages obtained directly on brannerite (550-572 Ma, Ludwig and Cooper, 1984). In this sense, Crocker's Well uranium occurrence shares many analogies with Rössing and Limousin types (*e.g.* Cuney, 2010), with the exception of the sodic enrichment.

The Hidden Valley (HV) area is located at Brannerite Hill in the North Finders Ridge in south Central Australia. This area is characterized by Mesoproterozoic migmatitic gneisses associated with Neoproterozoic metasediments and volcanics (Coats

and Blissett, 1971), which recorded metamorphism related to the Delamerian orogeny (Foden *et al*., 2006). Palaeozoic leucogranites and pegmatites dated around 450 Ma are intrusive within this metamorphic sequence (Wülser, 2009). Among the pegmatite intrusions, one displays an alkaline syenite composition and includes albite, K-feldspar, quartz, biotite, alkaline amphibole and brannerite (Wülser, 2009). Other brannerite occurrences (not studied) are within quartz-ilmenite veins such as Charlotte and Jacob mineralizations characterized by large euhedral brannerite crystals (Wülser, 2009).

The El Cabril (EC) occurrence is located in the Sierra Albarrana, Andalusia (Spain). This massif belongs to the late Proterozoic to Lower Cambrian Ossa Morena zone and is mainly composed of paragneisses, micaschists and garnet-bearing amphibolites (González del Tánago and Arenas, 1991; Azor and Ballèvre, 1997). Metamorphic rocks are cross cut by pegmatite intrusions, which are composed of quartz, K-feldspar, albite, muscovite, tourmaline, garnet, biotite, monazite, ilmenite, rutile and primary uranium minerals, such as brannerite and uraninite (Garotte *et al*., 1980; Contreras *et al*., 1983). Age of brannerite crystallization is unknown but is not older than the Devonian thermal event (351Ma - 391Ma) recorded by amphibolite and metapelite in the Sierra Albarrana (Dallmeyer and Quesada, 1992).

The Lodrino (BR1) pegmatite in Ticino, Switzerland crosscuts the Variscan orthogneisses of the Leventina Nappe (Rütti *et al*., 2008) and is mainly composed of quartz and orthoclase, with minor albite, muscovite, brannerite, molybdenite, scheelite, apatite, titanite, powellite and rutile (Bianconi and Simonetti, 1967). Age of pegmatite emplacement is unknown, but it is probably related to the well-known Tertiary pegmatite field that extends over Southwestern Switzerland (Wenk, 1970; Burri *et al*., 2005). This area overlaps the zone of alpine migmatization and available U-Pb geochronological constrains span between 29 and 20 Ma (Guastoni *et al*., 2014). This age is significantly

1193 older than the K-Ar age at ca. 11.4 Ma reported for the Lengenbach brannerite
1194 mineralization in Eastern Valais (Purdy and Stalder, 1973; Graeser and Guggenheim,
1195 1990).

1196 Sample NA12 is a single crystal from a pegmatite collected along the Marienfluss
1197 Valley, to the West of Hartmann Mountains, Northern Namibia. This pegmatite is intrusive
1198 within the Paleoproterozoic Epupa Metamorphic Complex, made of migmatized granitoid
1199 gneisses with rare intercalations of metasediments (Kröner *et al*., 2010). This unit was
1200 intruded by Mesoproterozoic granitoids related to extension in the Southern Congo
1201 craton (Kröner and Rojas-Agramonte, 2017) and further experienced further
1202 overprinting due to the late Neoproterozoic to early Palaeozoic Pan-African event related
1203 to the Kaoko orogeny (Goscombe *et al*., 2003). This later event, characterized by
1204 polyphase deformation and magmatism has produced biotite-muscovite pegmatite dykes,
1205 especially in the Hartmann Mountains (Goscombe *et al*., 2005); sample (NA12) is spatially
1206 related to this ca. 500 Ma episode (Goscombe *et al*., 2005), but further studies are required
1207 to confirm this hypothesis.

1208

1209 TABLE A1 Standard used for calibration of EPMA analyses.

1210

1211 FIG. A1 Raman spectra of a synthetic brannerite and studied natural brannerite samples.
1212 The synthetic brannerite sample comes from Mesbah *et al*. (2019). The characteristic
1213 vibrational Raman modes of synthetic brannerite are at 760 cm^{-1} (antisymmetric
1214 stretching vibration of the (Ti-O-Ti) moiety), 195, and 159 cm^{-1} (lattice external modes,
1215 see Zhang *et al.* (2013) and Mesbah *et al.* (2019) for a complete assignment of the Raman
1216 vibration modes). Spectra of natural samples were acquired in unaltered domain (Figs
1217 3,6). Abbreviations: BA: Bou Azzer; KV: Kratka Valley; MC: Mont Chemin; HL: Himalaya;

GD: La Gardette; NA12: Namibia; CW: Crocker's Well; EC: El Cabril; HV: Hidden Valley; BR1: Lodrino.

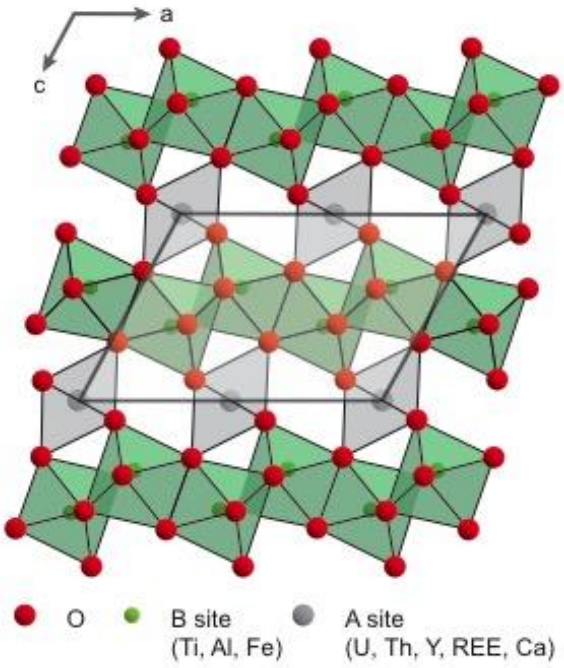

1221

1222 Figure 1

1223

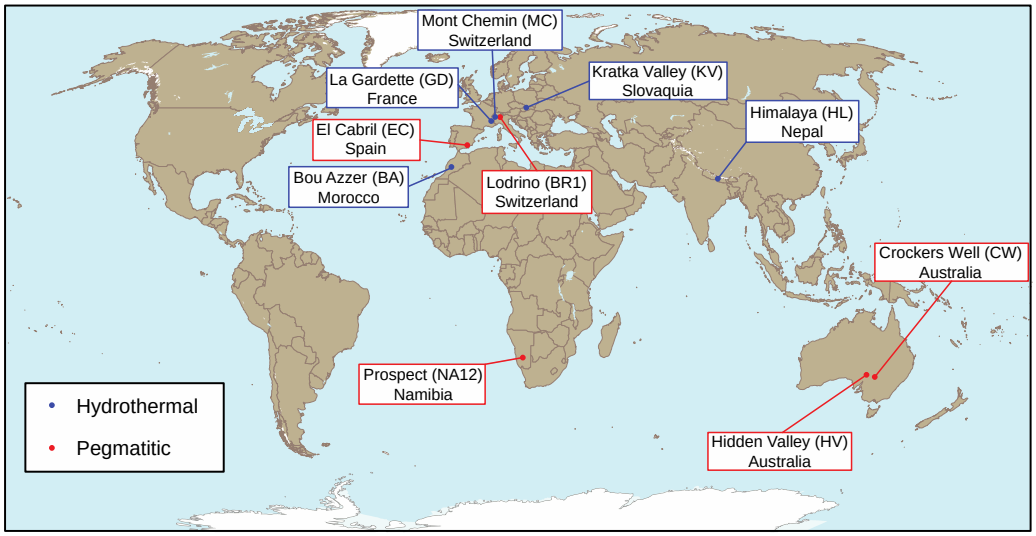

1224

1225 Figure 2

1226

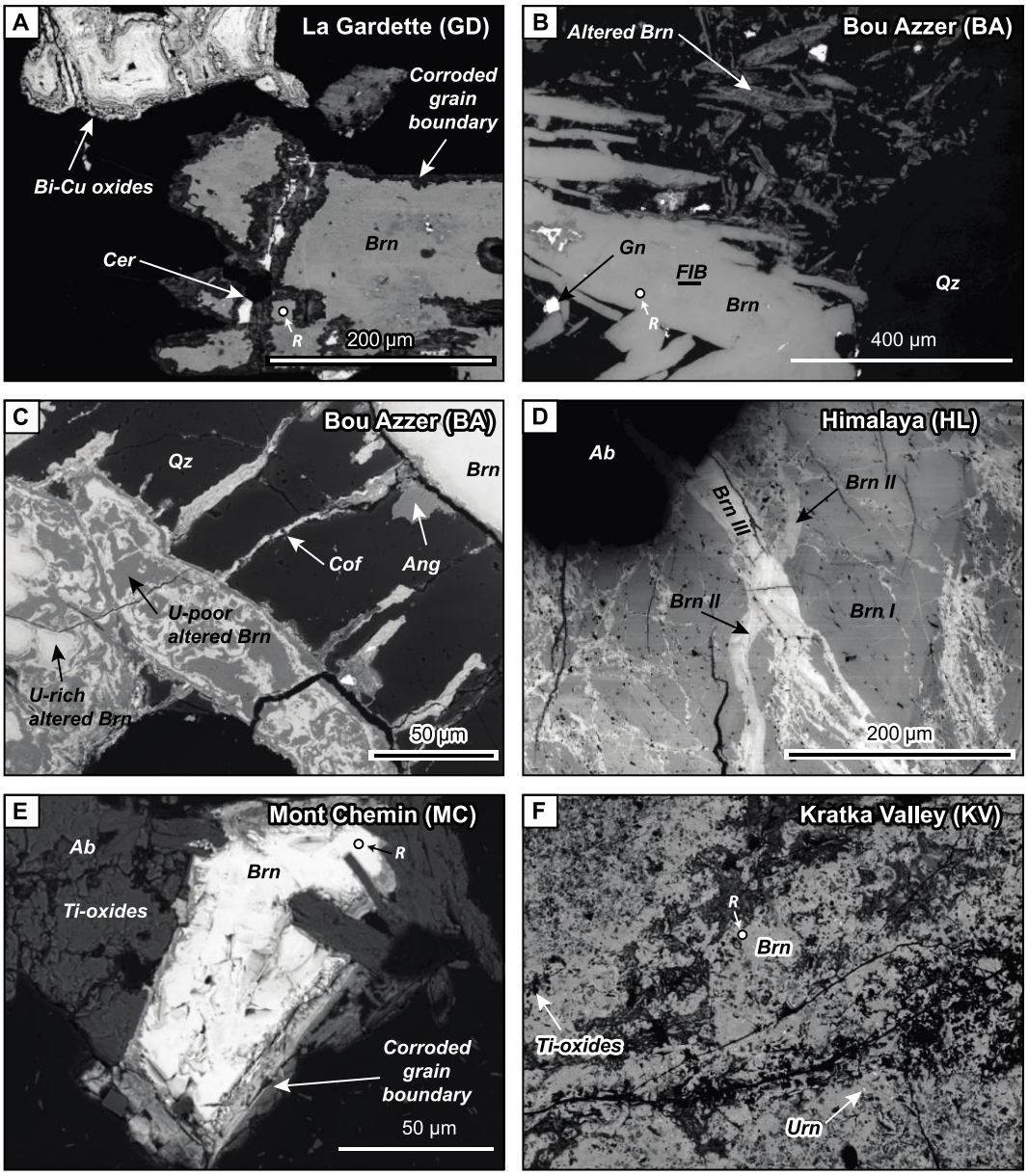

1227

1228 Figure 3

1229

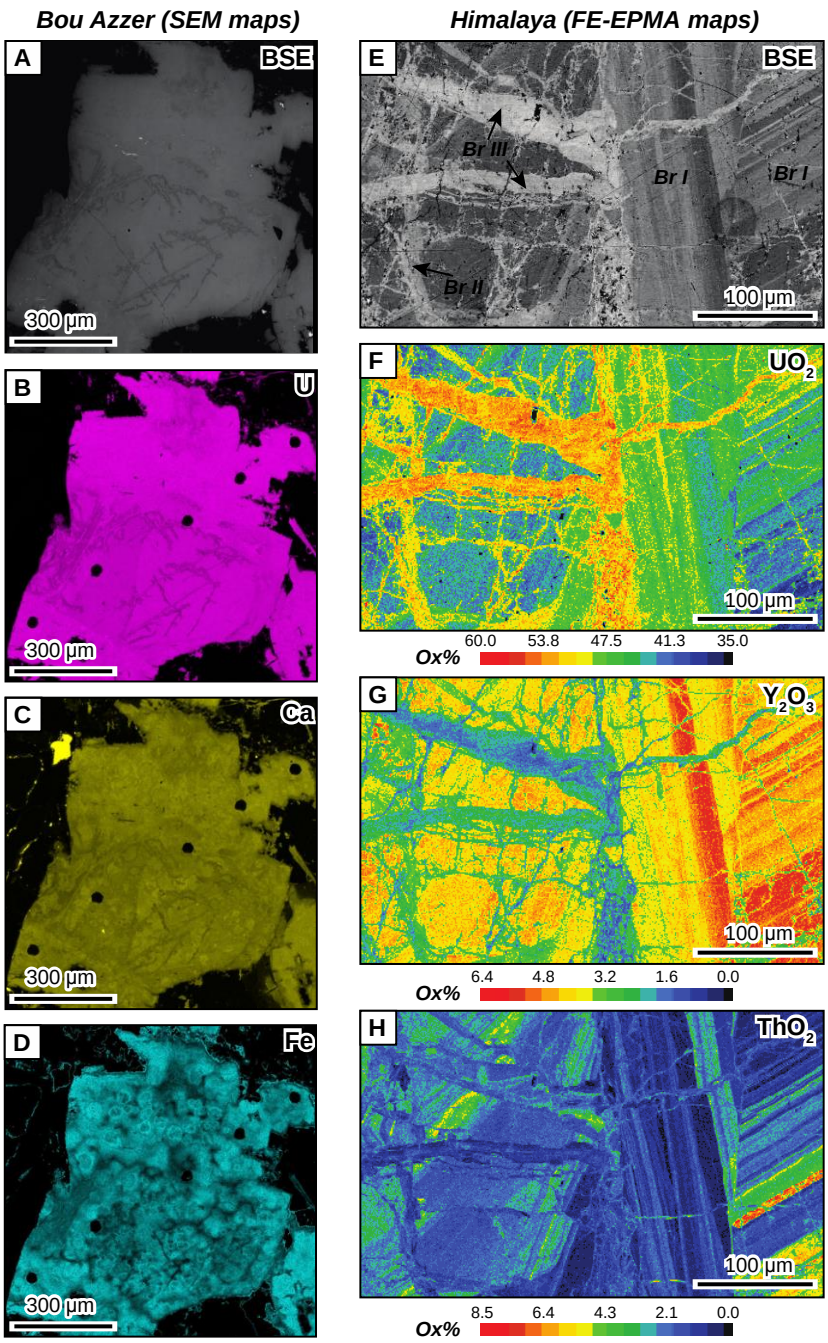

1230

1231 Figure 4

1232

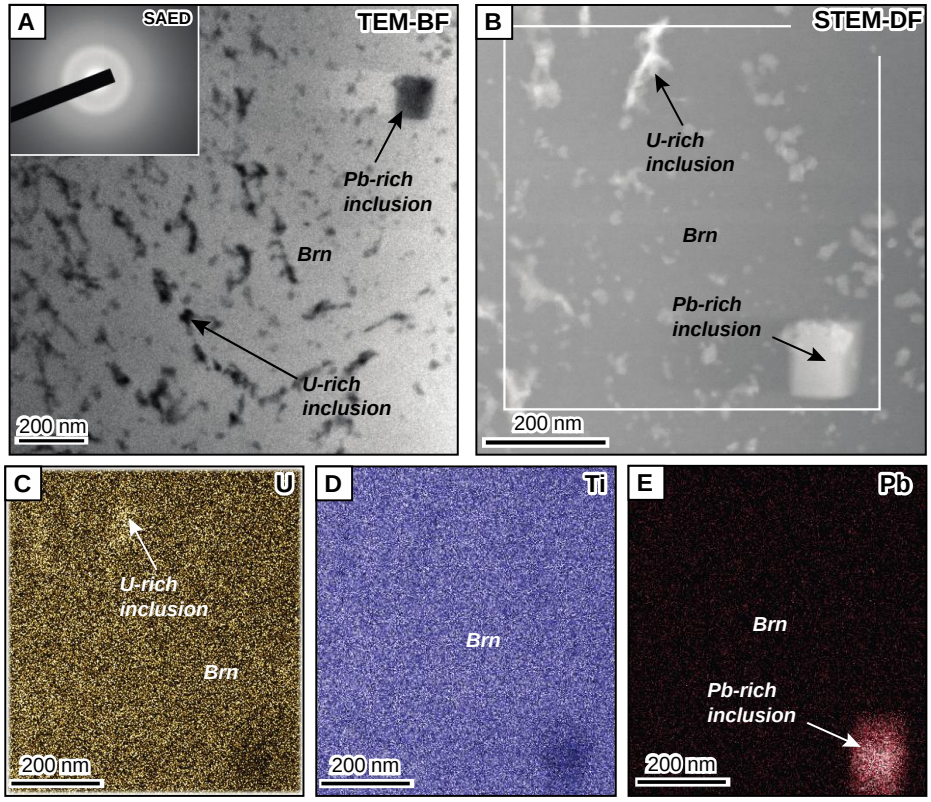

1233

1234 Figure 5

1235

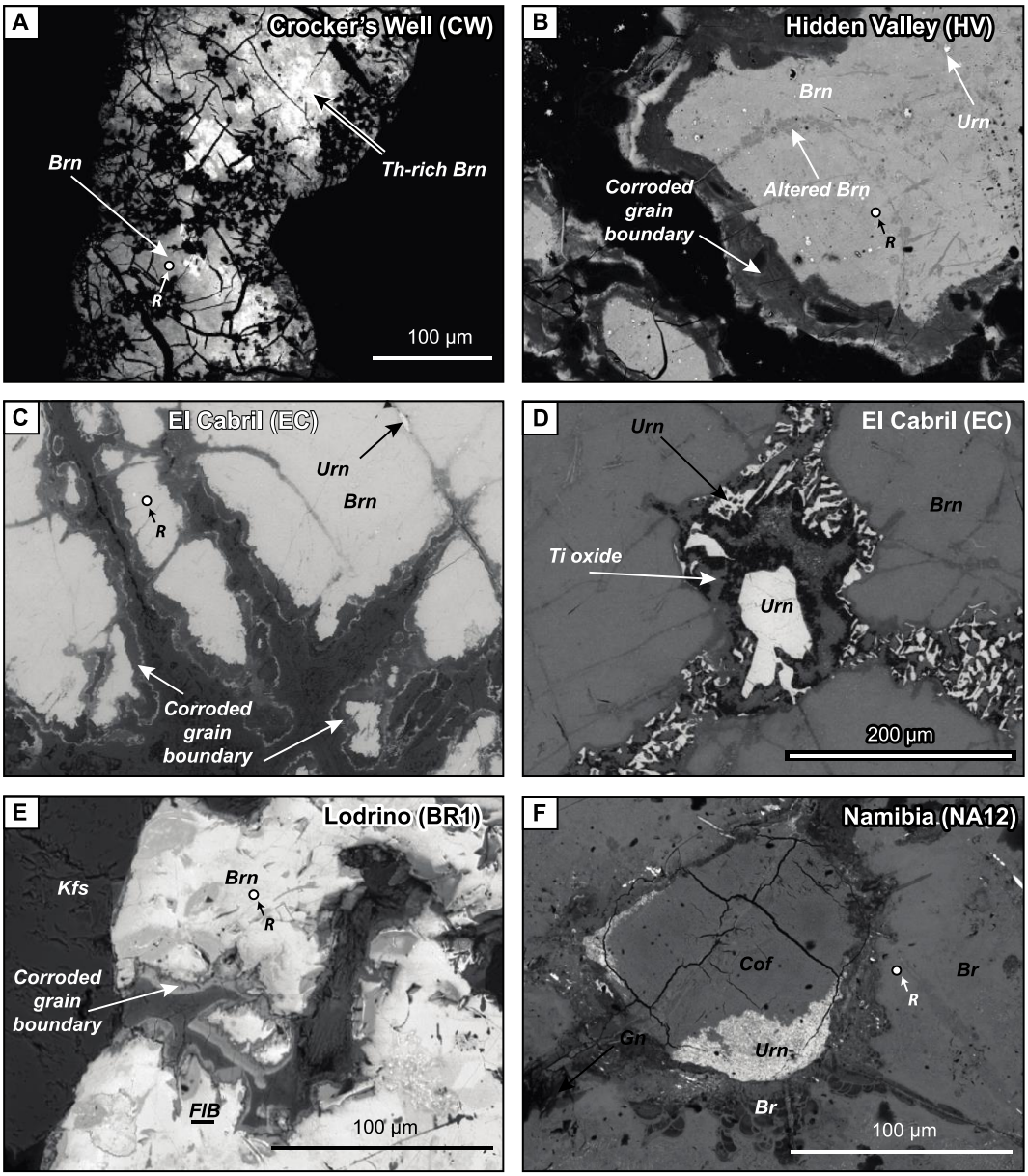

1236

1237 Figure 6

1238

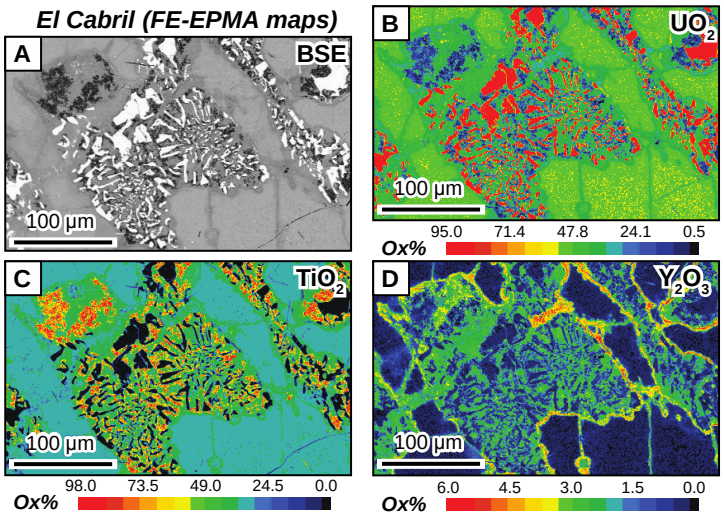

1239

1240 Figure 7

1241

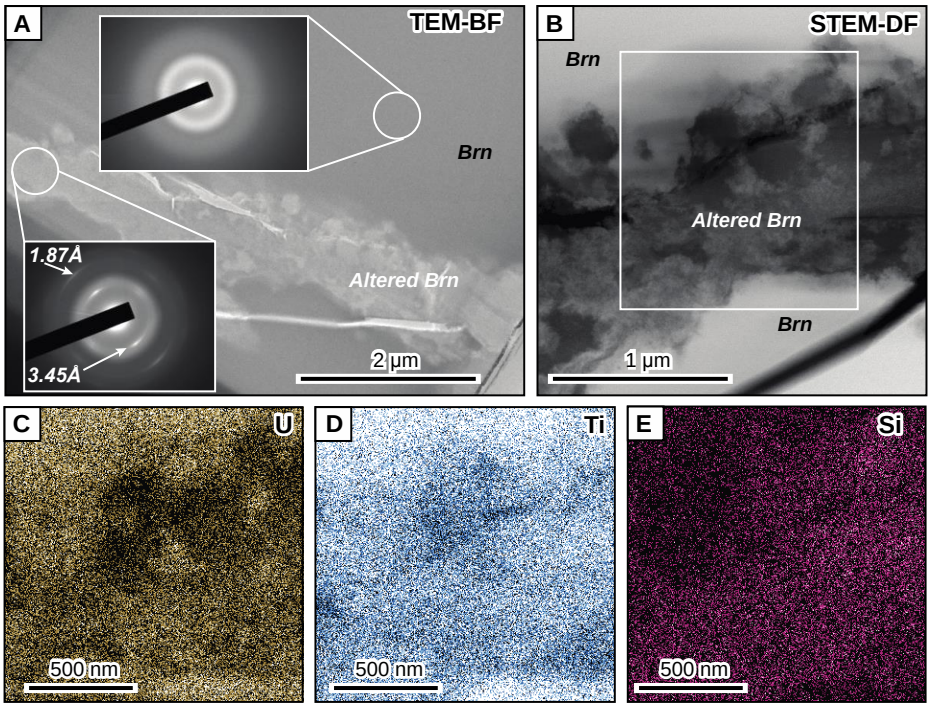

1242

1243 Figure 8

1244

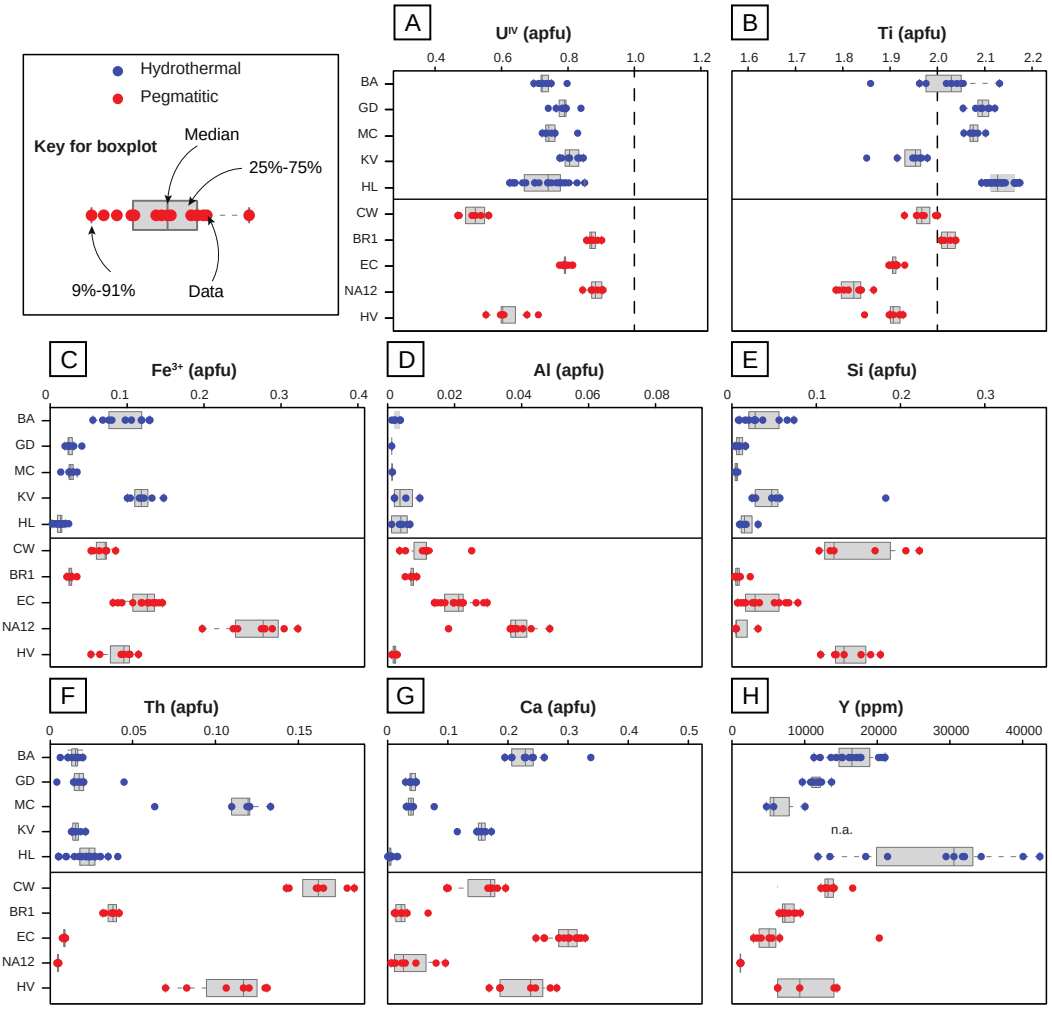

1245

1246 Figure 9

1247

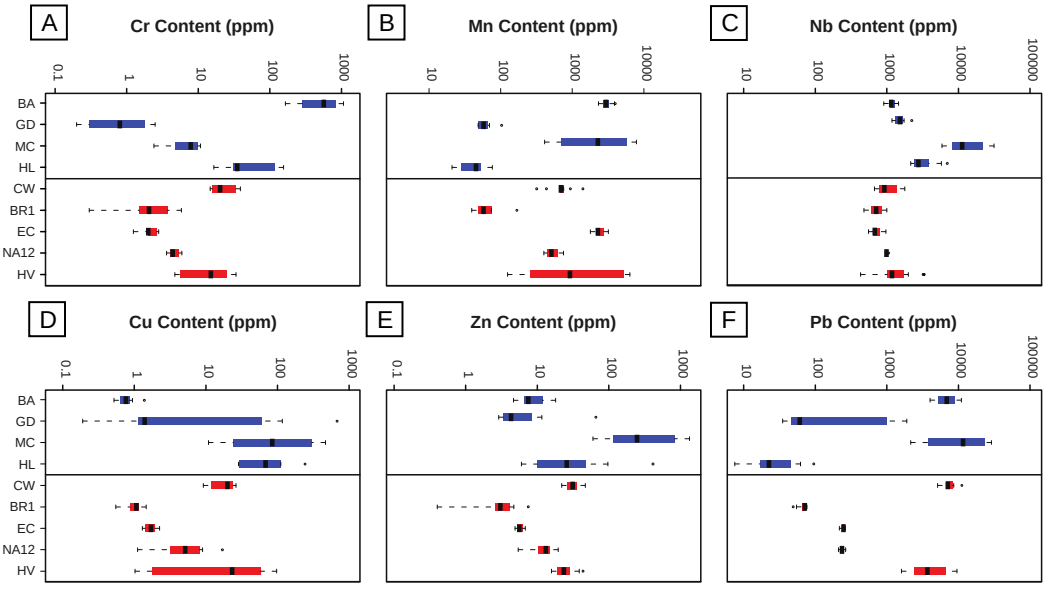
A
Cr Content (ppm)
B
Mn Content (ppm)
C
Nb Content (ppm)
D
Cu Content (ppm)
E
Zn Content (ppm)
F
Pb Content (ppm)
BA
GD
MC
HL
CW
BR1
EC
NA12
HV

Figure 10

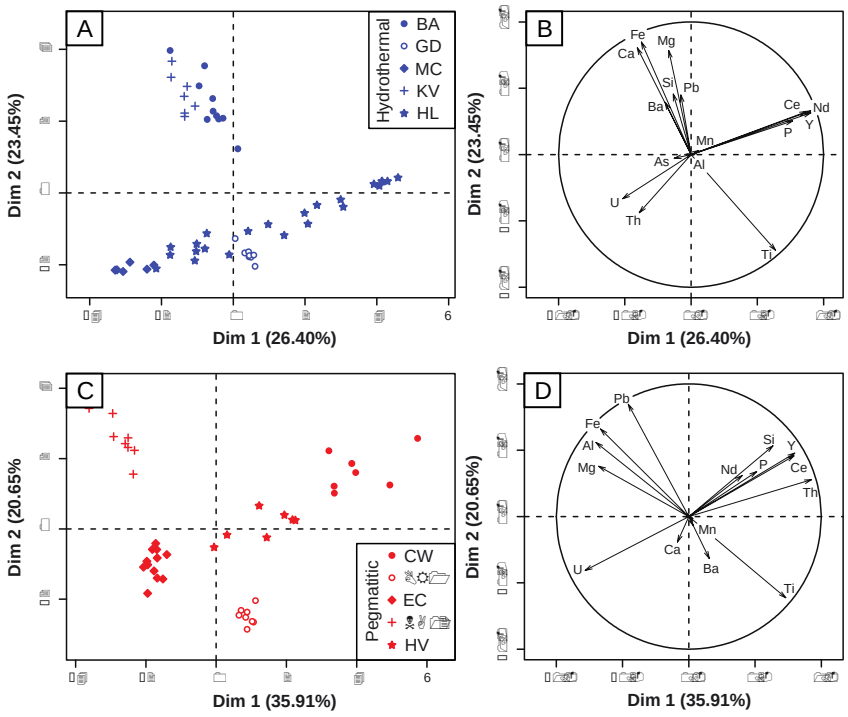

1251

1252 Figure 11

1253

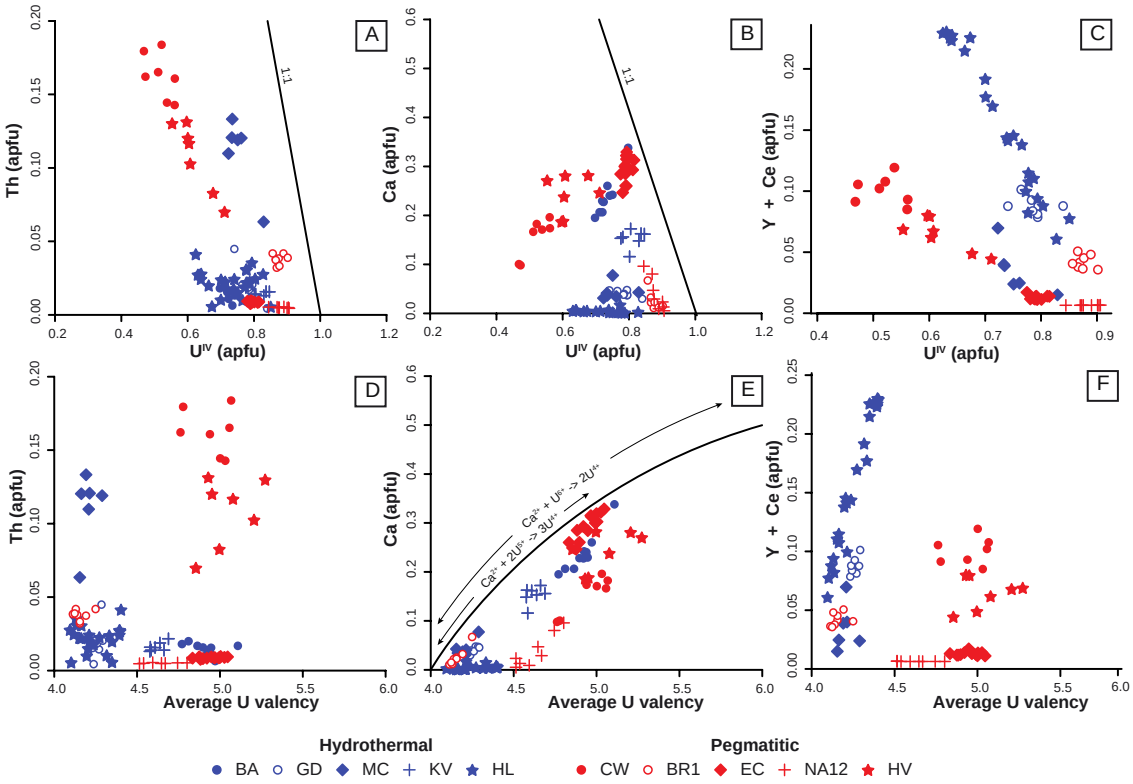

1254

1255 Figure 12

1256

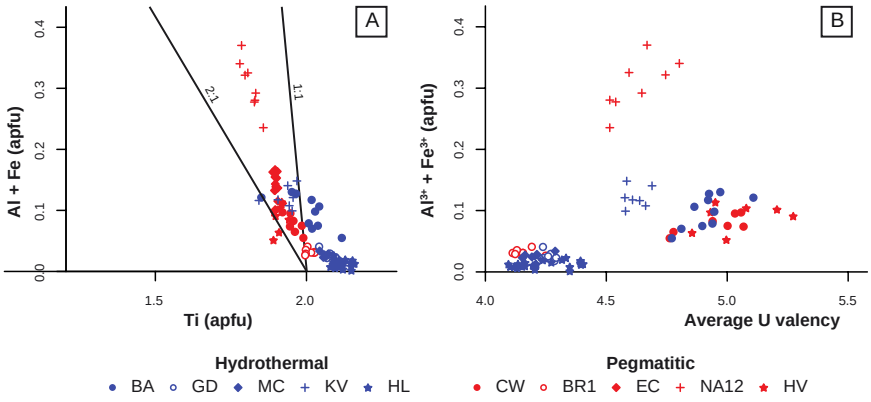

1257

1258 Figure 13

1259

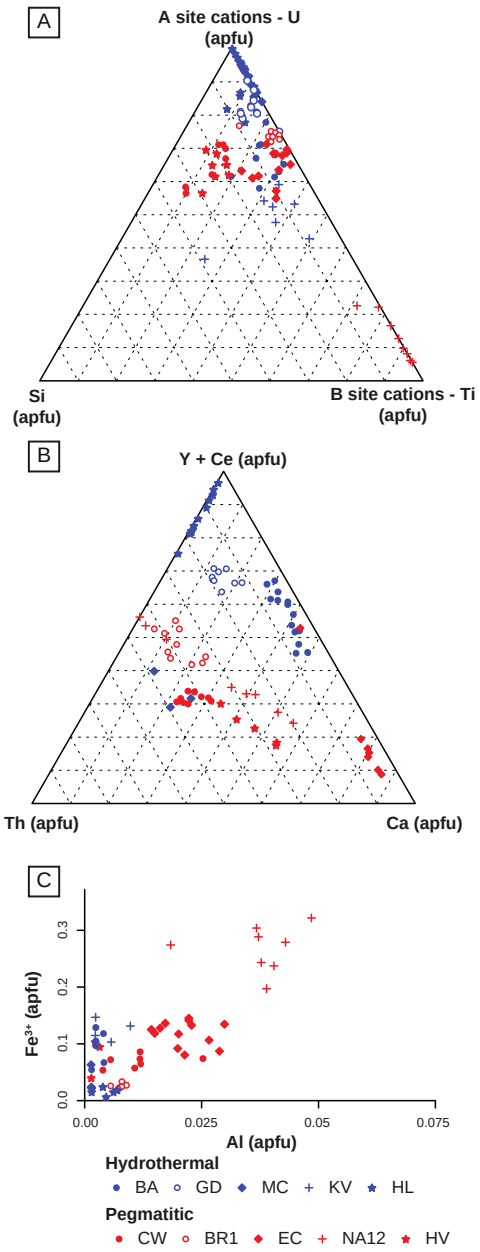

1260

1261 Figure 14

1262

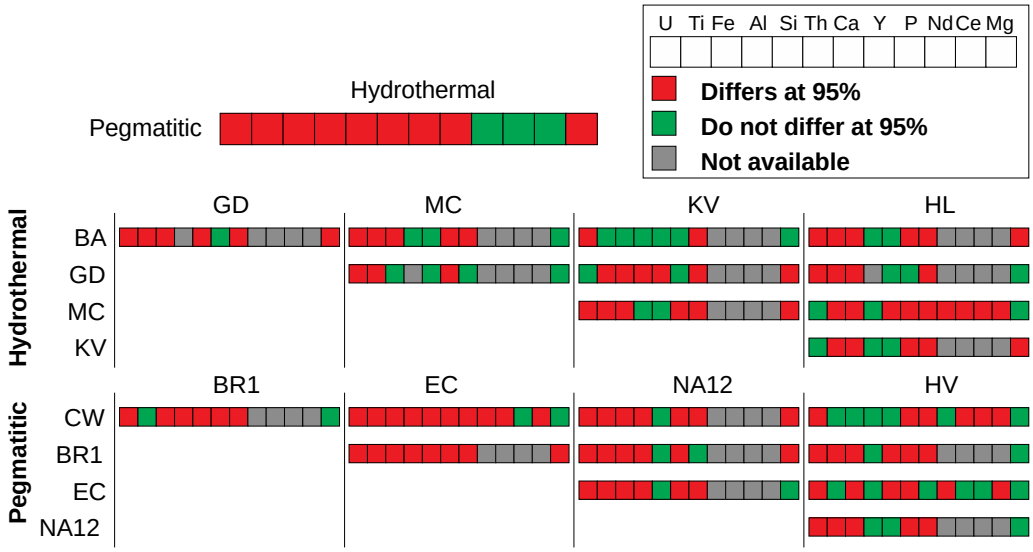

1263

1264 Figure 15

1265

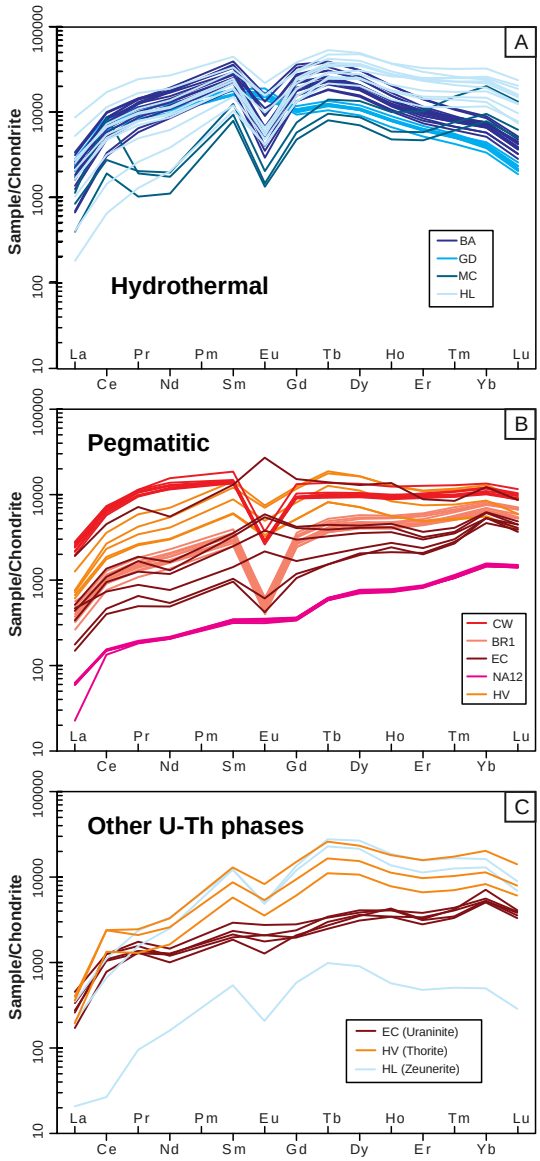

1266

1267 Figure 16

1268

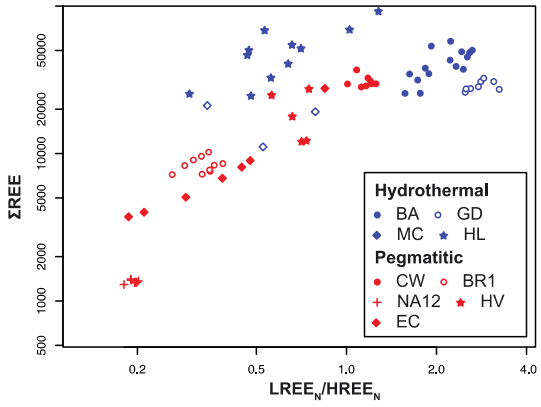

1269

1270 Figure 17
1271

	Hydrothermal Brannerite															Pegmatitic Brannerite														
Locality	Bou Azzer			La Gardette			Mont Chemin			Kratka Valley			Himalaya			Namibia			Hidden Valley			Crockers Well			Lodrino			El Cabril		
N	10			8			6			7			23			8			7			7			8			13		
Analyses (wt.%)	Min - Max	Mean	SD	Min - Max	Mean	SD	Min - Max	Mean	SD	Min - Max	Mean	SD	Min - Max	Mean	SD	Min - Max	Mean	SD	Min - Max	Mean	SD	Min - Max	Mean	SD	Min - Max	Mean	SD	Min - Max	Mean	SD
UO_2	43.56 – 51.81	46.54	2.12	49.96 – 57.01	53.42	1.85	47.92 – 54.07	49.36	2.14	49.88 – 54.5	52.53	1.40	42.74 – 57.55	49.65	4.35	54.08 – 56.46	55.11	0.85	37.93 – 46.53	41.23	3.10	31.58 – 37.17	34.46	2.07	55.91 – 57.49	56.85	0.48	51.41 – 53.16	52.30	0.50
TiO_2	35.56 – 39.12	37.67	0.89	41.01 – 42.45	41.78	0.48	39.06 – 41.14	39.90	0.70	35.37 – 37.74	36.97	0.75	40.97 – 43.83	42.65	0.81	33.02 – 33.97	33.49	0.36	36.96 – 38.67	37.75	0.59	37.6 – 39.64	38.48	0.68	37.67 – 39.29	38.66	0.58	36.34 – 37.51	37.07	0.35
SiO_2	0.08 – 1.01	0.47	0.30	n.d. – 0.2	0.08	0.07	n.d. – 0.5	0.01	0.02	0.3 – 2.75	0.84	0.80	n.d. – 0.42	0.04	0.10	n.d. – 0.4	0.06	0.13	1.5 – 2.62	2.06	0.38	1.47 – 3.37	2.19	0.72	0.01 – 0.027	0.071	0.079	0.05 – 1.11	0.49	0.34
Al_2O_3	n.d. – 0.04	0.015	0.015	n.d. – 0.01	0.003	0.004	n.d. – 0.01	0.002	0.004	n.d. – 0.11	0.03	0.04	n.d. – 0.08	0.01	0.02	0.21 – 0.57	0.44	0.10	n.d. – 0.03	0.009	0.011	0.04 – 0.31	0.14	0.08	0.06 – 0.1	0.085	0.011	0.17 – 0.37	0.26	0.06
Fe_2O_3*	1 – 2.43	1.82	0.49	0.36 – 0.8	0.51	0.13	0.24 – 0.64	0.48	0.12	1.91 – 2.81	2.28	0.29	0.02 – 0.44	0.23	0.10	3.6 – 5.96	4.95	0.73	1.02 – 2.22	1.70	0.40	1.02 – 1.64	1.31	0.19	0.39 – 0.64	0.48	0.07	1.57 – 2.82	2.32	0.40
CaO	2.53 – 4.56	3.14	0.54	0.42 – 0.66	0.57	0.08	0.43 – 1.04	0.60	0.21	1.56 – 2.3	2.06	0.22	n.d. – 0.23	0.06	0.06	0.07 – 1.28	0.50	0.42	2. 36 – 3. 92	3.13	0.59	1.36 – 2.7	2.14	0.49	0.15 – 0.91	0.35	0.23	3.37 – 4.55	4.04	0.35
BaO	0 – 0.14	0.08	0.04	0.02 – 0.11	0.07	0.03	n.d.			0.15 – 0.31	0.23	0.05	n.d.			0 – 0.08	0.045	0.029	n.d.			n.d.			n.d. – 0.08	0.026	0.034	n.d.		
MnO	0.26 - 0.47	0.36	0.06	n.d.			n.d.			0.15 – 0.32	0.23	0.06	n.d.			0.02 – 0.11	0.058	0.035	n.d.			n.d.			n.d. – 0.01	0.001	0.003	n.d.		
MgO	0.02 – 0.1	0.06	0.03	0.01 – 0.02	0.018	0.004	0.02 – 0.03	0.023	0.005	0.04 – 0.08	0.059	0.016	n.d. – 0.03	0.008	0.010	0.05 – 0.09	0.069	0.012	0.02 – 0.06	0.039	0.015	0.01 – 0.05	0.029	0.012	0.01 – 0.04	0.026	0.009	0.03 – 0.09	0.061	0.016
Y_2O_3	n.d.			1.23 – 1.74	1.47	0.14	0.26 – 1.69	0.77	0.48	n.d.			1.52 – 4.7	3.26	1.01	0.14 – 0.15	0.15	0.003	0.78 -1.71	1.28	0.31	1.33 – 2.01	1.71	0.21	0.82 – 1.2	0.99	0.12	0.17 – 0.37	0.23	0.03
Ce_2O_3	n.d.			0.58 – 0.82	0.70	0.07	0.17 – 0.31	0.23	0.05	n.d.			0.19 – 1.84	0.88	0.56	0.01 – 0.01	0.014	0.001	0.39 – 0.56	0.45	0.07	0.72 – 0.9	0.83	0.05	0.07 – 0.12	0.09	0.01	0.16 – 0.26	0.19	0.02
Nd_2O_3	n.d.			0.68 – 0.88	0.79	0.07	0.04 – 0.15	0.07	0.04	n.d.			0.13 – 1.47	0.74	0.46	0.01 – 0.02	0.015	0.0003	0.18 – 0.37	0.27	0.06	0.59 – 0.93	0.75	0.11	0.09 – 0.16	0.12	0.02	n.d. – 0.01	0.001	0.003
PbO	0.19 – 1.73	1.06	0.49	0.06 – 0.07	0.065	0.005	n.d.			0.43 – 0.82	0.60	0.12	n.d.			2.99 – 4.04	3.62	0.34	n.d.			n.d.			0.08 – 0.16	0.108	0.022	n.d.		
ThO_2	0.4 – 1.25	0.92	0.23	0.29 – 2.96	1.29	0.71	4.04 – 8.5	7.10	1.43	0.83 – 1.35	1.02	0.19	0.35 – 2.75	1.48	0.58	0.27 – 0.33	0.30	0.02	4.47 – 8.71	7.08	1.47	9.22 – 11.99	10.57	1.02	2.05 – 2.67	2.39	0.20	0.49 – 0.62	0.57	0.04
Σoxides	88.85 – 96.99	92.11	1.98	99.04 – 102.67	100.76	1.13	97.57 – 99.28	98.52	0.66	94.55 – 99.66	96.85	1.66	96.79 – 102.96	98.99	1.83	97.97 – 99.56	98.81	0.51	93.39 – 96.91	95.00	1.06	90.43 – 94.39	92.61	1.24	99.53 – 101.03	100.27	0.47	96.1 – 98.93	97.52	0.84
Brannerite formula (apfu) - based on 4O																														
U(IV)	0.7 – 0.8	0.732	0.026	0.74 – 0.84	0.787	0.026	0.72 – 0.83	0.755	0.035	0.78 – 0.85	0.811	0.025	0.62 – 0.85	0.730	0.067	0.844 – 0.906	0.883	0.020	0.553 – 0.711	0.617	0.052	0.468 – 0.562	0.519	0.035	0.856 – 0.902	0.875	0.014	0.775 – 0.815	0.793	0.011
Ca	0.19 – 0.34	0.237	0.038	0.03 – 0.05	0.040	0.006	0.03 – 0.08	0.044	0.016	0.12 – 0.17	0.153	0.017	0 – 0.02	0.004	0.004	0.005 – 0.096	0.038	0.032	0.169 – 0.281	0.225	0.041	0.098 – 0.196	0.156	0.037	0.011 – 0.067	0.026	0.017	0.247 – 0.329	0.295	0.025
Ba	0 – 0.004	0.002	0.001	0 – 0.003	0.002	0.001	-	-	-	0 – 0.01	0.006	0.001	-	-	-	0 – 0.002	0.001	0.001	-	-	-	-	-	-	0 – 0.002	0.001	0.001	-	-	-
Mn	0.02 – 0.03	0.021	0.004	-	-	-	-	-	-	0.01 – 0.02	0.014	0.004	-	-	-	0.001 – 0.007	0.004	0.002	-	-	-	-	-	-	0 – 0.001	0.000	0.000	-	-	-
Mg	0 – 0.01	0.006	0.003	0 – 0.002	0.002	0.000	0.002 – 0.003	0.002	0.000	0 – 0.01	0.006	0.002	0 - 0.003	0.001	0.001	0.005 – 0.010	0.007	0.001	0.002 – 0.006	0.004	0.002	0.001 – 0.005	0.003	0.001	0.001 – 0.004	0.003	0.001	0.003 – 0.009	0.006	0.002
Pb	0 – 0.03	0.020	0.009	0 – 001	0.001	0.000	-	-	-	0.01 – 0.02	0.011	0.002	-	-	-	0.056 – 0.079	0.070	0.007	-	-	-	-	-	-	0.001 – 0.003	0.002	0.000	-	-	-
Th	0.01 – 0.02	0.015	0.004	0 – 0.04	0.019	0.011	0.06 – 0.13	0.111	0.022	0.01 – 0.02	0.016	0.003	0.01 – 0.04	0.022	0.009	0.004 – 0.005	0.005	0.000	0.070 – 0.131	0.108	0.022	0.143 – 0.184	0.163	0.015	0.032 – 0.042	0.038	0.003	0.008 – 0.010	0.009	0.001
Y	-	-	-	0.04 – 0.06	0.052	0.005	0.01 – 0.06	0.028	0.017	-	-	-	0.05 – 0.16	0.114	0.035	0.0056 - 0.0059	0.006	0.000	0.029 – 0.062	0.046	0.011	0.048 – 0.074	0.062	0.008	0.031 – 0.044	0.037	0.005	0.006 – 0.011	0.008	0.001
Ce	-	-	-	0.03 – 0.04	0.036	0.003	0.006 – 0.01	0.007	0.002	-	-	-	0.01 – 0.08	0.039	0.024	0.0007 - 0.0008	0.001	0.000	0.015 – 0.023	0.018	0.003	0.034 – 0.046	0.039	0.003	0.004 – 0.007	0.006	0.001	0.004 – 0.006	0.005	0.001
Nd	-	-	-	0.03 – 0.04	0.039	0.003	0.002 - 0.005	0.003	0.002	-	-	-	0.01 - 0.06	0.032	0.019	0.0007 - 0.001	0.001	0.000	0.007 – 0.015	0.012	0.003	0.027 – 0.047	0.036	0.006	0.005 – 0.009	0.008	0.001	0 - 0.001	0.000	0.000
Σ A-site	0.96 – 1.2	1.033	0.062	0.93 – 0.97	0.939	0.012	0.94 – 0.97	0.948	0.012	0.98 – 1.06	1.017	0.029	0.89 – 0.93	0.910	0.010	0.991 – 1.042	1.015	0.015	0.921 – 1.095	1.018	0.053	0.840 – 1	0.941	0.065	0.965 – 1.012	0.986	0.016	1.055 – 1.154	1.116	0.031
(excl. U)	0.259 - 0.398	0.302	0.037	0.214 - 0.273	0.240	0.022	0.138 - 0.283	0.228	0.046	0.174 - 0.227	0.206	0.017	0.152 - 0.504	0.333	0.115	0.107 - 0.184	0.138	0.027	0.405 - 0.539	0.464	0.043	0.466 - 0.587	0.522	0.040	0.127 - 0.196	0.153	0.022	0.286 - 0.367	0.336	0.025
Ti	1.85 – 2.12	2.004	0.066	2.04 – 2.11	2.081	0.019	2.04 – 2.09	2.064	0.014	1.84 – 1.97	1.930	0.040	2.08 – 2.16	2.119	0.024	1.78 -1.857	1.814	0.025	1.891 – 1.942	1.909	0.017	1.921 – 1.990	1.958	0.022	1.996 – 2.027	2.011	0.013	1.889 – 1.921	1.900	0.008
Al	0 – 0.003	0.001	0.001	0 – 0.001	0.000	0.000	0 – 0.001	0.000	0.000	0 – 0.01	0.002	0.003	0 – 0.01	0.001	0.002	0.018 – 0.048	0.037	0.008	0 – 0.002	0.001	0.001	0.003 – 0.025	0.011	0.006	0.005 – 0.008	0.007	0.001	0.014 – 0.029	0.021	0.005
Fe(III)	0.05 – 0.13	0.097	0.025	0.02 – 0.04	0.025	0.006	0.01 – 0.03	0.025	0.007	0.10 – 0.15	0.119	0.015	0 – 0.02	0.011	0.005	0.197 – 0.322	0.268	0.038	0.052 – 0.114	0.086	0.020	0.052 – 0.084	0.067	0.010	0.020 – 0.033	0.025	0.004	0.080 – 0.145	0.119	0.020
Si	0.01 – 0.07	0.033	0.021	0 – 0.01	0.005	0.005	0 – 0.003	0.001	0.001	0.02 – 0.18	0.057	0.052	0 – 0.03	0.003	0.006	0 – 0.028	0.004	0.009	0.103 – 0.175	0.138	0.024	0.101 – 0.222	0.147	0.047	0.001 – 0.019	0.005	0.006	0.003 – 0.076	0.034	0.023
Σ B-site	2.03 – 2.18	2.135	0.041	2.08 – 2.13	2.112	0.013	2.08 – 2.1	2.090	0.009	2.07 – 2.14	2.108	0.028	2.09 – 2.17	2.134	0.024	2.093 – 2.155	2.123	0.020	1.073 – 2.202	2.134	0.042	2.139 – 2.250	2.183	0.044	2.028 – 2.063	2.048	0.012	2.044 – 2.116	2.073	0.020
(excl. Ti)	0.061 - 0.194	0.131	0.037	0.019 - 0.041	0.031	0.007	0.012 - 0.037	0.026	0.007	0.123 - 0.298	0.179	0.053	0.001 - 0.05	0.015	0.011	0.235 - 0.370	0.309	0.044	0.167 - 0.260	0.225	0.034	0.176 - 0.287	0.225	0.041	0.03 - 0.047	0.037	0.005	0.136 - 0.220	0.173	0.024
Σ REE	3.13 – 3.22	3.168	0.022	3.05 – 3.06	3.051	0.003	3.03 – 3.05	3.038	0.008	3.12 – 3.13	3.126	0.006	3.02 – 3.06	3.044	0.015	3.116 – 3.169	3.138	0.019	3.124 – 3.176	3.152	0.017	3.090 – 3.145	3.124	0.021	3.025 – 3.053	3.034	0.009	3.165 – 3.207	3.189	0.013
Av. U valency	4.771 - 5.108	4.92	0.09	4.232 - 4.293	4.26	0.02	4.154 - 4.289	4.20	0.04	4.577 - 4.689	4.62	0.04	4.095 - 4.403	4.25	0.11	4.514 - 4.802	4.63	0.10	4.855 - 5.273	5.04	0.14	4.762 - 5.068	4.95	0.12	4.113 - 4.250	4.16	0.04	4.834 - 5.046	4.95	0.06

Table 1

	Hydrothermal Brannerite												Pegmatitic Brannerite														
Locality	Bou Azzer			La Gardette			Mont Chemin			Himalaya			Namibia			Hidden Valley			Crockers Well			Lodrino			El Cabril		
N	15			8			3			11			8			5			9			10			7		
Analyses (pp	Min - Max	Mean	SD	Min - Max	Mean	SD	Min - Max	Mean	SD	Min - Max	Mean	SD	Min - Max	Mean	SD	Min - Max	Mean	SD	Min - Max	Mean	SD	Min - Max	Mean	SD	Min - Max	Mean	SD
Cr	218 – 1066	616.35	304.66	0.2 – 2.5	1.12	0.89	n.d.			16.5 – 155	73.98	54.96	3.6 – 5.9	4.69	0.79	21.3 – 33.6	27.54	4.86	14.7 – 38.8	22.68	8.49	0.3 – 5.8	2.60	1.78	1.5 – 2.7	1.96	0.44
Co	0.001 – 1.26	0.33	0.49	0.004 – 0.04	0.02	0.01	0.62 – 4.47	2.14	1.67	0.51 – 10.8	4.17	4.70	n.d. – 0.35	0.19	0.12	n.d.			2.8	2.8	0.00	0.002 – 0.79	0.15	13.99	0.129 – 2.7	0.19	0.05
Ni	0.5 – 6.1	3.25	1.66	0.7 – 4.8	2.10	1.91	n.d.			10.9	10.90	0.00	0.2 – 0.5	0.35	0.15	n.d.			n.d.			14 – 38	25.38	13.44	0.78 – 1.61	1.12	0.33
Cu	0.52 – 0.94	0.73	0.13	0.19 – 680	100.55	222.27	10.9 – 131.7	60.10	51.80	28.6 – 242.8	95.88	79.49	1.11 – 17	6.37	4.72	1.02 – 1.99	1.60	0.35	9.2 – 26.3	18.18	6.33	0.55 – 1.46	1.03	1.79	4.8 – 6.6	5.54	0.60
Zn	4.65 – 18	9.26	3.66	2.9 – 66	12.60	20.35	60 – 326	185.33	109.13	6 – 412	68.20	117.39	5.4 – 19.6	12.64	4.04	17.4 – 28.6	22.78	4.82	21.9 – 47	31.94	7.34	0.4 – 7.5	3.30	372.09	11.5 – 41.4	19.91	10.25
Nb	908 – 1456	1177.60	140.54	1180 – 2225	1555.50	305.12	5890 – 12270	9473.33	2663.36	2161 – 700	3483.82	1498.61	956 – 1058	991.25	28.99	1021 – 1332	1159.80	110.17	673 – 1780	1019.33	348.79	478 – 997	714.87	347.62	459 – 702	535.43	81.56
Mo	0.17 – 6.7	1.24	1.58	n.d. – 1.1	0.39	0.44	0.46 – 1.72	1.09	0.63	1.32 – 15.9	5.10	5.48	0.02 – 0.25	0.11	0.08	0.52 – 11.5	8.02	3.94	0.86 – 2.98	1.47	0.71	0.09 – 5.3	1.41	57.39	0.21	0.21	0.00
La	203.4 – 1042	593.49	234.80	622 – 1024	791.13	115.67	120.6 – 346	241.23	92.70	55.8 – 2727	827.15	730.27	7.02 – 19.43	17.30	3.90	190.1 – 389.2	248.66	71.91	604 – 866	753.00	85.84	79.6 – 171	119.97	35.95	45.6 – 623	179.07	185.26
Pr	706 – 1776	1345.73	342.06	1017 – 1396	1215.13	122.22	122.9 – 245.3	199.77	54.66	158.6 – 3042	1162.43	774.83	22.12 – 23.68	22.70	0.44	311 – 716	455.92	149.33	1157 – 1392	1287.22	80.44	128.8 – 217.3	173.50	455.40	51.8 – 663	188.07	199.02
Nd	5070 – 11610	8552.00	2011.73	5830 – 7540	6781.25	603.69	656 – 1165	952.00	215.93	1224 – 16460	6770.36	4077.64	122.8 – 130.2	125.53	2.36	1791 – 4203	2708.60	918.99	6880 – 9360	7720.00	702.98	796 – 1339	1058.90	259.18	283.9 – 3440	981.99	1028.70
Sm	3570 – 7680	5425.47	1231.58	3053 – 3590	3254.88	206.68	1534 – 2431	1925.67	374.92	2058 – 8930	4570.09	1915.76	61.3 – 67.8	64.98	1.94	1155 – 2789	1840.00	645.95	2627 – 3625	2841.33	288.33	476 – 748	598.60	286.75	167.3 – 2420	663.44	736.48
Eu	213 – 1182	528.09	270.92	1016 – 1394	1164.38	104.58	97 – 148.1	117.13	22.22	305.6 – 1641	676.58	431.02	22.98 – 25.9	24.56	0.87	237.1 – 547.3	381.94	129.88	191.1 – 271.4	211.20	22.26	28.48 – 44.6	35.97	355.19	24.5 – 1505	362.57	479.74
Gd	3447 – 9370	5699.67	1718.85	2409 – 3040	2694.38	171.62	1227 – 1940	1551.33	294.61	3478 – 10160	5972.27	1994.46	87 – 94.6	90.55	2.72	1334 – 3211	2202.80	801.34	2338 – 3434	2548.11	324.48	614 – 903	733.90	277.50	221.5 – 3240	906.93	982.34
Tb	857 – 1862	1263.73	304.53	497 – 640	573.38	37.64	377.8 – 664	497.93	121.27	1048 – 2594	1681.09	462.27	27.49 – 29.39	28.39	0.73	385.6 – 889	619.94	214.23	436 – 649	488.89	59.00	167 – 240.8	195.94	651.06	68.7 – 682	206.16	200.15
Dy	4860 – 10020	6958.00	1524.62	2930 – 3851	3437.75	238.30	2240 – 4320	3117.00	879.89	6690 – 16290	11166.36	2957.82	225.3 – 247	235.11	6.18	2287 – 5290	3744.60	1332.55	3000 – 4310	3285.22	377.35	1257 – 1811	1472.60	587.20	560 – 3920	1317.43	1094.89
Ho	728 – 1474	1016.53	217.10	475 – 640	566.75	42.41	342 – 717	493.67	161.26	1027 – 2738	1892.55	531.20	51.8 – 56.2	53.58	1.37	401.7 – 919	646.62	230.20	635 – 892	691.78	74.80	279.7 – 396.9	327.35	361.00	121.2 – 753	261.41	205.91
Er	1541 – 2987	2139.87	399.31	1082 – 1435	1284.38	92.24	974 – 2137	1440.67	501.80	2476 – 7050	4732.09	1355.20	170 – 182.5	176.04	3.55	1026 – 2345	1655.00	580.39	1912 – 2657	2097.00	211.45	899 – 1238	1027.30	429.29	406 – 1910	753.57	487.23
Tm	198.3 – 353.7	266.56	40.94	136.3 – 178.6	163.01	11.76	196.9 – 493	311.97	129.57	377 – 1062	698.16	194.62	34.07 – 37.17	35.11	1.02	165 – 379.1	265.20	92.51	304.9 – 417	333.78	33.79	159.3 – 225	185.85	636.88	84.2 – 289	130.46	66.23
Yb	1065 – 1860	1445.13	201.70	694 – 918	823.63	63.23	1625 – 4220	2608.33	1148.80	2476 – 6930	4424.09	1272.49	300.2 – 326.4	309.68	8.30	1159 – 2689	1862.60	649.66	2107 – 2820	2322.22	224.01	1246 – 1687	1441.80	636.09	782 – 2000	1064.29	391.23
Lu	90.1 – 165.9	126.02	19.41	59.5 – 82	69.54	6.45	159.7 – 426	261.57	117.37	241.7 – 779	476.32	162.73	44.9 – 48.3	46.31	1.13	127.5 – 300.2	205.82	73.18	280.9 – 373.1	307.78	28.98	164.6 – 222.4	187.51	62.16	110.6 – 285	150.33	56.49
Y	1290 - 21008	16639	3018	9690 - 13710	11602	1105	4750 - 10060	6850	2305	11820 - 4240(	27786.36	9721.75	1140 -1215	1168	25	6270 - 14460	10082	3586	12250 - 1661(	13601.11	1207.03	6470 - 9470	7642	935	2521 - 17500	5801	4884
Pb	98.1 – 360	180.59	76.64	35.1 – 14700	2118.53	4793.46	2160 – 17830	8456.67	6757.05	7.5 – 95	33.57	25.47	210.9 – 625.7	236.26	17.25	1600 – 3691	2724.20	800.21	5110 – 8620	6908.89	1121.89	49.1 – 76.5	67.93	8.61	202 – 262	233.81	21.11
ΣLREE/ΣHRE	1.57 - 2.64	2.12	0.36	2.5 - 3. 2	2.80	0.25	0.34 - 0.79	0.55	0.18	0.3 - 1.28	0.65	0.27	0.18 - 0.20	0.19	0.01	0.56 - 0.75	0.68	0.07	1 - 1.26	1.16	0.07	0.26 - 0.39	0.33	0.03	0.19 - 0.85	0.41	0.21

Table 2

Element	Standard formula	Diffraction Crystal	Analyzed radiation line	Counting time for peak (s)
U	UO2	PET	Mα	20
Ti	MnTiO3	LPET	Kα	20
Si	Albite	TAP	Kα	10
Al	Al2O3	TAP	Kα	10
Fe	Fe2O3	LIF	Kα	20
Ca	Andradite	PET	Kα	20
Ba	BaSO4	LIF	Lα	20
Mn	MnTiO3	LIF	Kα	20
Mg	Olivine	TAP	Kα	20
Y	YPO4	TAP	Lα	20
Ce	CePO4	LPET	Lα	20
Nd	NdPO4	LIF	Lα	20
Pb	PbS	LPET	Mα	20
Th	ThO2	PET	Mα	20

Figure A1

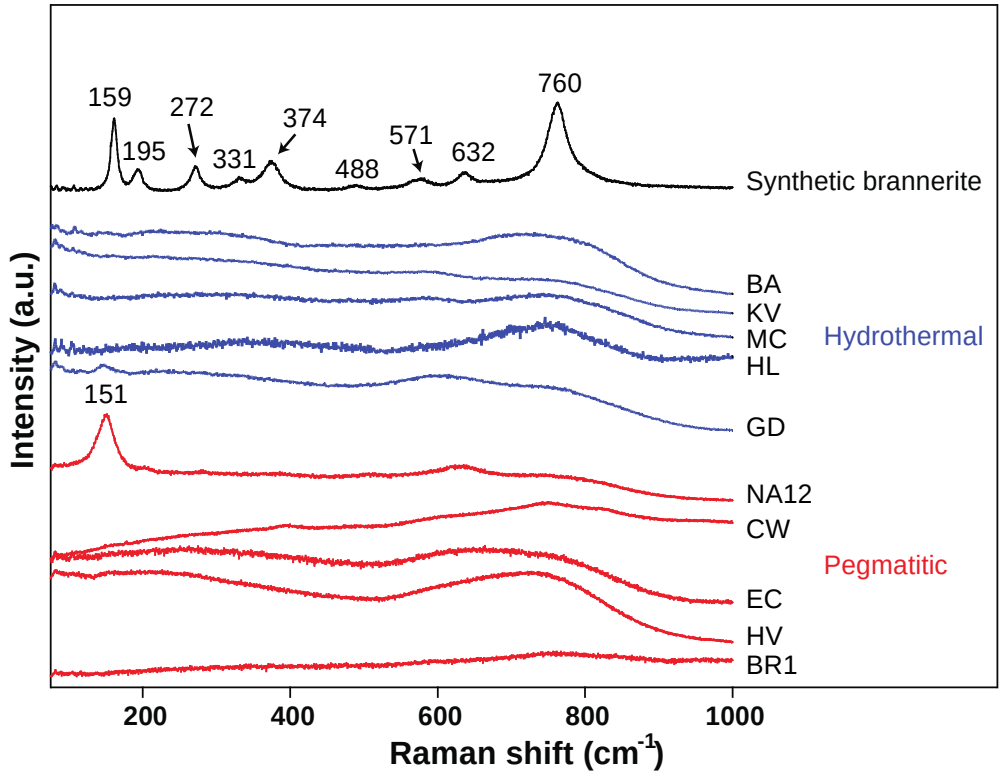
159
272
374
760
195
331
571
632
488
Synthetic brannerite
BA
KV
MC
HL
Hydrothermal
151
GD
NA12
CW
Pegmatitic
EC
HV
BR1
Intensity (a.u.)
200
400
600
800
1000
Raman shift (cm-1)

Figure A1